

1 **Seasonal asymmetries in the lag between insolation and surface temperature**

2 Aaron Donohoe*

3 *Polar Science Center, Applied Physics Lab, University of Washington*

4 Eliza Dawson

5 *Stanford University, Palo Alto, CA, USA*

6 Lynn McMurdie

7 *Department of Atmospheric Sciences, University of Washington, Seattle, WA, USA*

8 David S. Battisti

9 *Department of Atmospheric Sciences, University of Washington, Seattle, WA, USA*

10 Andy Rhines

11 *Netflix, Los Gatos, CA, USA*

12 *Corresponding author address: Applied Physics Lab, University of Washington, 1013 40th street,
13 Seattle, Washington/USA.

14 E-mail: adonohoe@u.washington.edu

ABSTRACT

15 We analyze the temporal **structure** of the climatological seasonal cycle in
16 surface air temperature across the globe. We find that, over large regions of
17 the Earth, the seasonal cycle of surface temperature departs from an annual
18 harmonic: **the** duration of fall and spring **differ** by as much as two months. We
19 characterize this asymmetry by the **metric** ASYM, defined as the phase lag of
20 the seasonal maximum temperature relative to the summer solstice minus the
21 phase lag of the seasonal minimum temperature relative to winter solstice. We
22 present a global analysis of ASYM from weather station data and atmospheric
23 reanalysis and find that ASYM is well represented in the reanalysis. ASYM
24 generally features positive values over land and negative values over the ocean
25 indicating spring has a longer duration over the land domain whereas fall has
26 a longer duration over the ocean. However, ASYM also features more pos-
27 itive values over North America compared to Europe and negative values in
28 the polar regions over ice sheets and sea ice. **Understanding the root cause of**
29 **the climatological ASYM will potentially further our understanding of con-**
30 **trols on the seasonal cycle of temperature and its future/past changes.** We ex-
31 plore several candidate mechanisms to explain the spatial structure of ASYM
32 including: (i) modification of the seasonal cycle of surface solar radiation by
33 the seasonal evolution of cloud thickness; (ii) **differences in the seasonal cycle**
34 **of the atmospheric** boundary layer depth **over ocean and over land**; and (iii)
35 temperature advection by the seasonally evolving atmospheric circulation.

36 1. Introduction

37 The climatological seasonal cycle of surface (2m) daily average air temperature (hereafter T_{2m})
38 in the extratropics is forced by the seasonal cycle of insolation and moderated by atmospheric ad-
39 vection and radiative damping (North and Coakley 1978; Donohoe and Battisti 2013). Throughout
40 the extratropics, seasonal variations in insolation are nearly sinusoidal (Berger 1978). Hence, the
41 seasonal cycle of T_{2m} is well represented by the amplitude and phase of the annual harmonic
42 (Wallace and Osborn 2002; Thomson 1995; McKinnon et al. 2013). The spatial structure of the
43 amplitude and phase of the annual harmonic in T_{2m} provide insights into the underlying climate
44 processes including:

- 45 • the large amplitude of T_{2m} in the high latitudes driven by the large magnitude of seasonal
46 variations in insolation (Von Hann and Ward 1903; Peixoto and Oort 1992);
- 47 • the small amplitude and large phase lag in T_{2m} over the oceans due to the high heat capacity
48 of the ocean mixed layer and the efficient thermal coupling between T_{2m} and sea surface
49 temperature (SST; Prescott and Collins 1948);
- 50 • the large amplitude and small phase lag of T_{2m} over continental regions far downwind of
51 the ocean due to the small heat capacity of the land surface and atmospheric boundary layer
52 relative to that of the ocean mixed layer (Brooks 1917).

53 In addition, continental regions that are downwind of the ocean represent a mixture of the phase
54 and amplitude of T_{2m} between the above mentioned marine and continental cases (Stine et al.
55 2009).

56 Additional insights into the processes driving the seasonal cycle have been gleaned from the
57 spatial patterns of the change in the phase and amplitude of the annual harmonic of T_{2m} and
58 atmospheric temperature due to global warming that include:

- 59 • reduced amplitude and delayed phase of T_{2m} in regions where sea ice melt exposes the atmo-
60 sphere to the thermal reservoir of the ocean (Dwyer et al. 2012);
- 61 • enhanced amplitude and reduced phase lag (Donohoe et al. 2013) of mid-tropospheric tem-
62 perature due to enhanced shortwave absorption in the atmospheric column associated with
63 atmospheric moistening (Donohoe and Battisti 2013);
- 64 • phase changes in T_{2m} over land are moderated by the strength of mixing between marine and
65 continental air associated with annular mode changes (Stine and Huybers 2012).

66 Finally, the spatial pattern of observed changes in the annular harmonic of T_{2m} provide a de-
67 tectable fingerprint of anthropogenic forcing (Santer et al. 2018).

68 Are there additional insights to be gleaned from the climatological seasonal cycle in T_{2m} that
69 extend beyond the amplitude and phase of the annual harmonic? For example: is the cooling of
70 the surface air temperature in the fall more rapid than the warming in the spring? Is the answer the
71 same over the ocean and land domains or between the different continents? Annual harmonic anal-
72 ysis is poorly suited to answer these questions because the cold and warm seasons are constructed
73 to be symmetric in amplitude, duration and timing.

74 For illustrative purposes, consider the seasonal cycle of T_{2m} at Seattle-Tacoma international
75 airport (SEATAC; Fig. 1) that inspired this work – due in part to the authors’ familiarity with this
76 region. The minimum temperature of the smoothed seasonal cycle (see methods in Section 2B)
77 occurs on January 4th, 14 days after the winter solstice (the timing of the T_{2m} extrema and solstices
78 are shown by the vertical black and red lines, respectively) whereas the maximum temperature
79 occurs on August 4th, 44 days after the summer solstice. This (30 day) seasonal asymmetry of
80 the temperature lag (hereafter ASYM) relative to insolation suggests that the seasonal warming
81 into the peak of summer takes almost 2 months longer than the seasonal cooling into the peak of

82 winter. This point is visualized by comparing the observed seasonal cycle of T_{2m} to an annual
83 harmonic fit to the data (c.f. the thick black line to the thick dashed blue line in Fig. 1). The rate
84 of cooling (warming) during the autumn (spring) is far greater (less) than that expected from the
85 annual harmonic. The annual harmonic analysis of T_{2m} cannot capture these substantial seasonal
86 timing asymmetries and instead produces a phase of temperature that splits the differences between
87 the phase of the maximum and minimum.

88 Departures of T_{2m} from the annual harmonic that are characterized by ASYM have received little
89 attention in the literature but have the potential to provide new insights into the physics of climate
90 and its future changes. van den Broeke (1998) note that T_{2m} over Antarctica has a significant
91 semi-annual component with a slow cooling of temperatures during the winter and fast warming
92 during the spring. This seasonality is understood to result from the seasonal “shape” of insolation
93 which follows the top half of a sine curve in the summer but flat-lines to zero during winter and
94 thus projects onto the higher order harmonics via Gibbs overshoot. May et al. (1992) produced a
95 global analysis of T_{2m} at 122 stations including the (separate) timing of the seasonal maximum and
96 minimum temperature during the smoothed seasonal cycle (see their Figs. 89 and 91). They noted
97 that T_{2m} departs from the annual harmonic in monsoonal regions where the onset of the monsoons
98 initiates cooling prior to the summer solstice (Hurley and Boos 2015) but commented little on the
99 large scale patterns of ASYM. **More recently, Sheridan Dodds et al. (2016) analyzed the timing of**
100 **minimum and maximum temperatures at weather stations in the United states as well at trends in**
101 **the seasonal timing over the duration of the observational record.**

102 The purpose of this manuscript is threefold: (i) to present a comprehensive **global** analysis of the
103 climatological ASYM from historic station observations; (ii) establish that the ASYM in observa-
104 tions is captured in the ERA-Interim reanalysis product and use the latter product to document the
105 global three dimensional structure of ASYM (including the seasonal cycle of temperature in the

106 troposphere above the boundary layer); and (iii) explore possible physical mechanisms that govern
107 the global structure of ASYM.

108 2. Data and methods

109 a. Data sets

110 **Station Data:** Historical station data of near surface (2 meter) air temperature from the Global
111 Historical Climatology Network (GHCN Peterson and Vose 1997) is the primary source of data
112 used in our analysis. This data set has daily maximum (T_{MAX}) and minimum temperature (T_{MIN})
113 for nearly 100,000 stations with some stations reporting nearly continuous data for 175 years and
114 others containing less than 1 year of data. We thin the number of stations used in our analysis
115 using the following criteria: (i) for stations within 0.1 degrees (latitude and longitude) of each
116 other, we remove all data except the longest continuous record – this eliminates locations that have
117 registered secondary or tertiary data; (ii) stations with less than 20 years of data are eliminated; (iii)
118 stations that have less than 5 years of data on any calendar day are eliminated; and (iv) stations
119 equatorward of 25° latitude for which the seasonal cycle is small in magnitude and more semi-
120 annual in nature are eliminated. These criteria reduce the number of stations to 3,096 stations
121 dispersed globally across land areas. We analyze the seasonal cycle of T_{2m} which is defined as
122 the average of T_{MAX} and T_{MIN} . While this method of averaging is biased relative to true time-
123 averages, it is recommended for the sake of consistency when comparing historical datasets such
124 as station observations that often only provide daily extrema (World Meteorological Organization
125 2011). All results presented here are nearly unchanged if we analyze the seasonal timing of T_{MAX}
126 or T_{MIN} in isolation.

127 ASYM is also calculated from in situ surface air temperature (and sea surface temperature –
128 SST) data at marine stations. Marine observations come from Ocean Weather ships that were
129 deployed in the World War II era by the UK (Downes 1977) and United States of America (US
130 Weather Bureau 1977) at fixed locations primarily in the North Atlantic but secondarily in the
131 North Pacific. T_{2m} and SST records of sufficient length to define a smoothed climatological sea-
132 sonal cycle were retrieved from Stations Alpha, Bravo, Charlie, Delta, Echo, India, Juliet, Kilo
133 and, Mike in the Atlantic, and Stations Extra, Hotel, Nan, Papa (Belka et al. 2014) and Victor in
134 the Pacific.

135 Additionally, in situ data from Washington state is used to analyze the seasonal timing of temper-
136 ature and surface solar radiation. ASYM is calculated from near surface air temperature data from
137 Mount Rainier (D’Amico 2019), Washington, USA (Paradise Ranger Station, altitude 5,400 feet
138 and Camp Muir Climbing camp, altitude 10,188 feet). Finally, we also examine the seasonal cycle
139 of total, direct and diffuse solar radiation measured on the roof of the Department of Atmospheric
140 Sciences at the University of Washington in Seattle, approximately 15 miles from SEATAC air-
141 port (there is no solar data at SEATAC); these data have been measured at 1 minute intervals since
142 2000.

143 **Gridded Temperature Data:** While our primary focus here is on ASYM derived from histor-
144 ical observations, we demonstrate that the regional structure of ASYM seen in the station data is
145 well represented in the reanalysis data which allows for a spatially continuous global analysis of
146 ASYM. We consider two sets of daily reanalysis temperature data: the ERA Interim (Dee et al.
147 2011) 1000 hPa temperature at a resolution of 1.5° latitude (or roughly 150 km), and the NCEP
148 reanalysis 2 meter air temperature at a resolution of 2° latitude (or roughly 200 km). Results using
149 the higher resolution ERA data are shown in the manuscript figures; results using NCEP are shown
150 in the appendix (Fig. A2). The ERA reanalysis product we use spans the time period 1979-2015

151 and the NCEP data spans 1970-2012. The primary conclusions are insensitive to the choice of
152 reanalysis product.

153 In some instances, geographic features that are smaller than the ERA-Interim gridbox can intro-
154 duce differences between the seasonal cycle of T_{2m} (and potentially ASYM) measured at stations
155 and its representation at the nearest ERA-Interim gridbox. For example, shown in the lower panel
156 of Fig. 1 is the T_{2m} from the Seattle station data (SEATAC) and the temperature from the ERA
157 reanalysis gridbox that includes Seattle. The temporal “shape” of the seasonal evolution of T_{2m}
158 and the timing of the maximum and minimum are nearly identical in the ERA and station data (c.f.
159 the vertical blue and black lines that are nearly on top of each other). However, in absolute terms,
160 the seasonal range of temperature is significantly greater in the ERA data. This absolute mis-
161 match should be expected from the approximately 150 km horizontal resolution of the ERA data
162 because the gridbox that includes Seattle also extends across the Cascade mountains into Central
163 Washington. Thus, the ERA gridbox that includes Seattle also includes the town of Ellensburg,
164 Washington located east of the Cascade Mountains. The February average minimum temperature
165 is 19°F (-7°C) in Ellensburg and 35°F (2°C) in Seattle. Thus, we should not expect absolute agree-
166 ment between the reanalysis and station data – especially in the presence of sharp sub-grid scale
167 topographic features. However, we show below that, in general, the spatial structure of ASYM
168 primarily varies at the continental scale and, thus, the reanalysis data is well suited for assessing
169 its spatial variability. Given the strong correspondence between the large scale patterns of ASYM
170 in the surface station temperature data and surface reanalyses products, we can use the reanalysis
171 data to probe the vertical structure of ASYM.

172 **Solar Radiation data:** The seasonal phasing of the surface solar radiation at the top of atmo-
173 sphere and at the surface is analyzed using satellite derived global gridded solar radiation data . We
174 use data from the Clouds and the Earth’s Radiant energy system experiment (CERES) SYN ver-

175 sion 4 (Kato and Coauthors 2018; Loeb and Coauthors 2018). The CERES data is derived from
176 radiometer measurements on the Aqua and Terra satellites that are assimilated using a radiative
177 transfer model, resulting in a self consistent surface radiative flux measurements. This data set has
178 daily temporal resolution over the time period 2000-2018 and provides global gridded coverage at
179 1° spatial resolution.

180 **Sea Surface Temperature Data:** While our focus is on ASYM calculated from near surface air
181 temperature (T_{2m}), we supplement our analysis by calculating ASYM from daily SST data. SST
182 data is from NOAA High-resolution Blended Analysis Version 2 on a 0.25° global grid over the
183 time period 1981-2016 (Reynolds et al. 2007).

184 **Energy fluxes in the atmospheric and oceanic column:** The seasonal input of energy into the
185 atmospheric and oceanic columns is calculated using the methodology described in Donohoe and
186 Battisti (2013). These calculations use radiative fluxes at the top of atmosphere and surface from
187 the the Clouds and Earth's Radiant Energy System experiment 4.0 (CERES Loeb and Coauthors
188 2018; Kato and Coauthors 2018), atmospheric energy flux convergence and column energy ten-
189 dencies calculated from ERA reanalysis (Dee et al. 2011). The turbulent energy exchange between
190 the surface and the atmosphere as a residual of the atmospheric energy budget.

191 *b. Methodology for defining the seasonal asymmetry in the lag between T_{2m} and insolation*

192 The methodology for calculating the seasonal asymmetry of the temperature time lag (ASYM)
193 from both station based T_{2m} data and reanalysis data is described here. Smoothed climatological
194 seasonal cycles of T_{2m} are created by first plotting all years of daily data on a domain of days
195 past January first of that year (black dots in Fig. 1) padded periodically on both sides. A spline
196 with 6 evenly spaced knots within the year is fit to the data (thick black line). Then the *timing*
197 *of the temperature maximum* (τ_{MAX}) is defined as the number of days past the summer solstice

198 on which the smoothed T_{2m} reaches its maximum; similarly, τ_{MIN} is defined as the number of
199 days past the winter solstice on which the smoothed T_{2m} reaches its minimum. Hence, positive
200 values of τ_{MAX} and τ_{MIN} correspond to the T_{2m} extremes that lag the solstices, and negative values
201 correspond to T_{2m} extremes that precede the solstices. Finally, ASYM is defined as τ_{MAX} minus
202 τ_{MIN} . Positive values of ASYM correspond to a maximum T_{2m} that lags summer solstice more
203 than minimum T_{2m} lags winter solstice. Hence, a positive ASYM indicates a prolonged spring and
204 hurried autumn (i.e. in the same sense of the ASYM seen at SEATAC in Fig. 1); negative ASYM
205 indicates a hurried spring and prolonged autumn. ASYM is calculated using the spline fit to the
206 data because, even with 70 years of data (e.g. at the SEATAC station shown in the top of Fig. 1),
207 the climatological average for a given calendar day (thin black line) is fairly jumpy from day to
208 day due to random sampling of synoptic variability and this would cause the timing of the extrema
209 to have some random component about the longer time scale seasonal evolution of temperature.
210 We chose a spline with 6 knots because this choice removes the jumpy structure of the synoptic
211 variability while retaining the temporal structure of the seasonal evolution. Alternative choices for
212 the number of knots between 3 to 12 knots do not significantly change the results presented here.
213 The seasonal asymmetry in downward surface solar radiation is calculated using the same
214 methodology used to calculate the seasonal asymmetry of the temperature lag.

215 3. Global structure of ASYM

216 In this section, we present global maps of ASYM calculated from the comprehensive set of
217 surface station data and from ERA reanalysis. We also present the vertical structure of ASYM
218 derived from reanalysis and highlight some curious features.

219 *a. Correspondence between τ_{MAX} , τ_{MIN} and, ASYM calculated from station and reanalysis data*

220 **Maps of τ_{MAX} , τ_{MIN} and ASYM calculated using the station data and calculated using the the**
221 **ERA reanalysis data are shown in Fig. 2. Dots represent the station values and the underlying col-**
222 **ors represent the ERA values. For each of the three quantities, values calculated from the station**
223 **data are in very good agreement with those calculated using the ERA reanalysis data (particularly**
224 **over land where it is difficult to discern the two). We quantify the correspondence between the**
225 **station based metrics and those calculated in the ERA reanalysis using the mean absolute differ-**
226 **ence between the station calculation and that in the nearest-neighbor ERA gridpoint. The mean**
227 **absolute difference is 3.7 days in τ_{MAX} , 4.0 days in τ_{MIN} and 4.4 days in ASYM. The spatial**
228 **correlation between station based and ERA based metrics is 0.84 for τ_{MAX} , 0.86 for τ_{MIN} and,**
229 **0.86 for ASYM. A scatter plot of ASYM calculated at each station versus that calculated from the**
230 **nearest neighbor ERA reanalysis gridpoint (Fig. A1) shows strong correlation with a slope near**
231 **1, a small ERA offset in ASYM (ASYM in the station data is 2.2 days greater than that in ERA**
232 **on average). The largest mismatch between station and nearest-neighbor ERA ASYM is found at**
233 **island weather stations where the station based ASYM is small or slightly positive whereas the**
234 **nearest neighbor ERA gridpoint is dominated by ocean and has a negative value (theses stations**
235 **account for the points far above the 1:1 line with negative ERA ASYM values in Fig. A1). Similar**
236 **results (with slightly lower correlations and mean absolute differences) are found when the ERA**
237 **reanalysis is replaced with T_{2m} from the NCEP reanalysis product (Appendix Fig. A2). There are**
238 **large differences between ASYM calculated from the 14 ocean weather ship stations (OWS) data**
239 **and that found in the co-located ERA data: ERA based ASYM values are predominantly negative**
240 **over the ocean – with the exception of the western side of the ocean basins – whereas the OWS**

241 data features values of ASYM near zero or positive, especially in the North Atlantic. We return to
242 this discrepancy in the next section.

243 Given the good correspondence between ASYM identified in the surface reanalysis data and that
244 from the T_{2m} station observations at the regional scale, we will extend the analysis of ASYM into
245 the troposphere using the reanalysis data to help illuminate the relevant mechanisms that affect
246 ASYM. We note that, with the exception of several high altitude stations, we have very few direct
247 observational constraints on ASYM calculated above the surface and must rely on the reanalysis
248 products for this calculation.

249 *b. Surface timing of seasonal cycle*

250 In general, τ_{MAX} and τ_{MIN} both show short lags over continental regions and long lags over
251 marine regions (Fig. 2) – differences that are expected due to the large thermal inertia of the ocean
252 versus the small thermal inertia of land and ice (Stine et al. 2009; Hasselmann 1976).

253 Westerly winds advect ocean-influenced air onto the western side of the continents, resulting
254 in larger values of τ_{MAX} and τ_{MIN} on the western side of the continents than on the eastern side.
255 Characteristic values of τ_{MAX} and τ_{MIN} are around 50 days in the western continents and around
256 20 days in the interior and along the eastern edge of the continents (Fig. 2). Westerly winds advect
257 continental-influenced air over the western ocean basins, resulting in τ_{MAX} and τ_{MIN} values that
258 are around 40 days, shorter than those over the central and eastern ocean basin (≈ 80 days; Fig. 2)

259 In addition to the large-scale similarities in the spatial maps τ_{MAX} and τ_{MIN} associated with
260 the contrasting heat capacity of land and ocean, there are substantial regional scale differences
261 in τ_{MIN} and τ_{MAX} . Figure 2 features the expected gradient from large lags on the western side
262 of continents to smaller lags in the continental interior and east side of the continents especially
263 evident in τ_{MAX} over North America and Eurasia and in τ_{MIN} over northern Europe. In contrast

264 over North America τ_{MIN} *increases* gradually eastward with values around 10 days along the west
265 coast of the US and values of around 30 days on the east coast and even larger values around the
266 Great Lakes (Fig. 2b). Hence, the west-east gradient of τ_{MIN} is opposite of that seen in τ_{MAX}
267 and opposite of what is expected based on the advection of maritime air into the continents by the
268 climatological westerly winds. A similar feature is seen over the Southwest Europe with small
269 values of τ_{MIN} (≈ 10 days) just downwind of the Atlantic and τ_{MIN} increasing (to ≈ 40 days) in
270 eastern Europe.

271 There are pronounced differences between τ_{MAX} and τ_{MIN} in the high latitudes of both hemi-
272 spheres. τ_{MAX} has small values over ice covered regions (≈ 10 -20 days), especially over the
273 Greenland and Antarctic ice sheets while τ_{MIN} has large values (≈ 60 days). **The small values of**
274 **τ_{MAX} are likely** due to the poor conduction of **heat** through ice which effectively isolates the atmo-
275 sphere from the underlying surface and, additionally, to the fact that temperature in the marginal
276 ice zone are pegged near the freezing point in the summer. The larger values of τ_{MIN} result from
277 gradual cooling during the polar night until the sun rises again in the spring. **Over northern India,**
278 τ_{MAX} has values of less than -20 days indicating that the maximum in T_{2m} leads the summer sol-
279 stice by more than 20 days whereas τ_{MIN} in the same region is of order +20 days as one might
280 expect from a continental interior. We argue below that the ASYM in this region is a consequence
281 of the onset of the monsoon which results in thick cloud cover that halts the seasonal warming.

282 The seasonal asymmetries in the lag between T_{2m} and insolation are best highlighted by the
283 metric ASYM (Fig. 2c). In both the station data and reanalysis data, **ASYM typically** shows:

- 284 • negative values over the ocean domain, indicating the winter minimum in T_{2m} is delayed more
285 than the summer maximum (exceptions include the northwestern Pacific, **North Atlantic south**

286 of Greenland, Gulf of Mexico, the west coast of Africa and the New Zealand sector which is
287 discussed further in the appendix);

- 288 • positive values over land, indicating that summer maximum temperatures lag more than win-
289 ter minimum temperatures (with the exception of northern Europe which shows little differ-
290 ence between τ_{MAX} and τ_{MIN});
- 291 • positive values of order 30 days over western North America that are in contrast to the near
292 zero values in the same latitudes over western Europe, even though both regions are down-
293 wind of the ocean and are characterized by a maritime climate;
- 294 • negative values in the Indian Monsoon region due to τ_{MAX} preceding the summer solstice;
295 and
- 296 • negative values in the high latitudes of both hemispheres due to the long delay of winter
297 minimum temperatures relative to the delay of the summer maximum.

298 The spatial pattern of ASYM is continental in scale and has magnitudes are of order 30 days (Fig
299 2c), comparable in magnitude to the seasonal asymmetry seen in Seattle, and corresponding to a
300 two month difference between the length of autumn and spring. Largest positive ASYM values are
301 found primarily on the west coast of North America (particularly in California) with ASYM values
302 in San Diego, Long Beach, Santa Barbara, San Luis Obispo and San Francisco all exceeding 40
303 days. The largest negative values of ASYM are found at stations in Antarctica and India with
304 values less than -50 days (offscale in Fig. 2) in five Antarctica stations including the South Pole
305 and four stations in India.

306 *c. Vertical structure of seasonal cycle timing*

307 **Immediately** downwind of the ocean, advection of air that has been influenced by interaction
308 with the ocean surface damps the seasonal amplitude of T_{2m} and increases the phase lag. This
309 advection occurs primarily in the mid and upper troposphere where zonal winds are strongest and,
310 **hence**, the amplitude (see Fig. 8 of Donohoe and Battisti 2013) and phase of atmospheric temper-
311 ature **above the boundary layer** are **more** zonally **homogenous** (see Fig. 3 of Stine and Huybers
312 2012) **than at the surface**. In order for **zonal advection** to influence T_{2m} overland, the upper level
313 seasonal temperature tendencies must be communicated downward via turbulence and radiative
314 heating¹. A central result from the previous section – positive ASYM over the western conti-
315 nents – **requires** that near surface zonal advection and/or the subsequent vertical communication
316 from the mid-troposphere to the surface does not operate symmetrically for seasonal cooling and
317 warming; we examine the vertical structure of ASYM to understand why.

318 The land-ocean contrast in τ_{MAX} that is prevalent at the surface is **nearly zonally** and vertically
319 invariant above the boundary layer with near uniform values around 45 days except for lower
320 values over the Arctic and Siberia (Fig. 3 left column and Fig. 4 top). The sharp gradient in τ_{MIN}
321 seen at the surface near the west coast of the United States is **present** throughout the troposphere.
322 Interestingly, the dipole between large τ_{MIN} to the west and small τ_{MIN} to the east over the western
323 United States at 400 hPa is shifted eastward relative to the surface dipole – so much so that along
324 130°W, τ_{MIN} aloft is delayed from that at the surface by almost 50 days. We speculate that the
325 upper level gradient in τ_{MIN} spanning the eastern Pacific Ocean and western US is caused by the
326 stationary high pressure ridge that is set up by the jet interacting with the Rocky Mountains during
327 December, January and, February (Held 2001; Eliassen and Palm 1961). Southerly advection of
328 warm air west of the ridge delays the seasonal minimum temperature until the ridge breaks down

¹This argument neglects the role of barotropic mountain waves

329 in February; similarly, northerly advection of cold air east of the ridge accelerates the cooling
330 leading to a phase advance of τ_{MIN} (i.e. $\tau_{MIN} < 0$).

331 There is also a north-south dipole in upper level (400 hPa) τ_{MIN} in both the North Pacific and
332 North Atlantic storm track regions with $\tau_{MIN} \approx 60$ days on the equatorward flank and τ_{MIN} of
333 approximately 30 days on the poleward flank (Fig. 3). We speculate this timing results from the
334 equatorward shift of the jet, storm track and baroclinity during the winter months (which is farthest
335 equatorward in February (Barnes and Simpson 2017): enhanced cooling propagates equatorward
336 with the equatorward migration of the storm track, thus the minimum temperature is delayed near
337 the equatorward limit of the storm track. The upper level τ_{MIN} in the Southern Hemisphere storm
338 track does not display the same equatorward-poleward dipole, perhaps because the seasonal move-
339 ment of the storm track is damped and more semi-annual in nature in the Southern Hemisphere
340 due to the strengthening and separation of the subtropical and sub-polar jets during the winter
341 (Trenberth 1991). Because the upper level map of τ_{MIN} has much more structure than that of
342 τ_{MAX} , upper level ASYM primarily reflects the structure in τ_{MIN} .

343 Fig. 4 shows longitudinal cross sections of the τ_{MAX} , τ_{MIN} and, ASYM, averaged across the lat-
344 itude band from 47°N to 57°N which was chosen to highlight the contrast in structure between the
345 west coast of North America and Europe (Fig. 4). As previously noted, above 700 hPa the zonal
346 profile of τ_{MAX} is much more homogenous than at the surface. Across Eurasia, τ_{MAX} is nearly
347 vertically invariant from the surface to the tropopause and has a value of approximately 30 days –
348 indicative of continental air. This result suggests that convection from the solar heated land mass
349 influences the upper atmosphere during the summer. Except for over the eastern Pacific Ocean,
350 τ_{MIN} is more zonally homogenous aloft than at the surface, with values of approximately 40 days.
351 The wintertime stationary wave generated by the Rocky Mountains is responsible for large (≈ 70
352 day) τ_{MIN} that extends vertically throughout the troposphere in the eastern Pacific. Interestingly,

353 this homogenized sector of high τ_{MAX} slants eastward with altitude and, thus, explains the reversal
354 of ASYM with height seen over the Pacific Northwest US.

355 Over the oceans, the vertical structure of τ_{MAX} in Fig. 4a shows a strong vertical gradient at
356 about 900 hPa with less delayed and vertically homogenous τ_{MAX} above 900 hPa. In contrast,
357 the vertical structure of τ_{MAX} over land is vertically homogenous from the surface all the way
358 through the troposphere suggesting some vertical communication between the surface and upper
359 atmosphere during the summer. The vertical structure of τ_{MIN} shows a strong vertical gradient
360 between 900 hPa and 700 hPa everywhere except over the eastern Pacific – suggesting that the
361 surface is isolated from the upper atmosphere over most regions during the winter.

362 Surface station data (circles circumscribed in white in Fig. 4) and marine observations (circles
363 circumscribed in gray) in the latitude band between 47°N to 57°N confirm the strong zonal gra-
364 dients seen in τ_{MIN} and ASYM in the reanalysis data including the following features: (i) the
365 strong gradient in τ_{MIN} seen along the West coast of North America; (ii) the increasing lag of τ_{MIN}
366 moving from the west coast of the US toward the interior and east coast; (iii) the large, continuous
367 gradient in τ_{MIN} between the ocean domain and land domain over northern Europe. Also shown in
368 Fig. 4 are τ_{MAX} , τ_{MIN} and, ASYM from the high altitude stations on Mount Rainier in Washington
369 state, USA (46.88°N, 121.7° W – plotted at the pressure level of the mean surface pressure at these
370 stations). Data from these stations show delays in τ_{MIN} that are greater than that at the surface and
371 closer to the values seen in the reanalysis atmospheric temperature at the same pressure. Specif-
372 ically, the T_{2m} at Camp Muir (680 hPa) has a prolonged cold season temperature with a delayed
373 τ_{MIN} (≈ 45 days) that is halfway between that at the same pressure in the reanalysis (≈ 60 days)
374 and that at the surface (≈ 20 days—Appendix Fig. A3).

375 4. Mechanisms of asymmetry in the seasonal cycle of temperature

376 We now explore several candidate mechanisms to explain the large scale patterns of climatolog-
377 ical ASYM and analyze the support for and shortcomings of each mechanism.

378 *a. Impact of clouds on the seasonal cycle of surface solar radiation*

379 The seasonal cycle of surface temperature is primarily driven by the amount of downwelling
380 solar radiation reaching the surface (DSR). DSR is a function of insolation at the top of atmosphere
381 – dictated by Earth-Sun geometry – and atmospheric shortwave transmissivity which is governed
382 by the concentration of atmospheric constituents that absorb (i.e. water vapor and ozone) and
383 reflect (i.e. clouds) solar radiation. Clouds play the dominant role in determining the spatial and
384 seasonal variability of atmospheric shortwave transmissivity (Taylor et al. 2007; Donohoe and
385 Battisti 2011). Here, we explore whether seasonal variations in cloud cover can explain the spatial
386 pattern of ASYM by way of modifying the seasonal timing of maximum and minimum DSR
387 relative to the insolation.

388 We consider the seasonal cycle of DSR observed in Seattle (Fig. 5a) as an illustrative example
389 and note at the outset that while the seasonal shape of T_{2m} in Seattle does follow (with uniform
390 lag) the seasonal evolution of DSR, this result is limited to the region and does not apply more
391 generally across the globe. Using the same periodic spline fit with 6 knots that was previously
392 applied to temperature, the date of maximum DSR is July 6th, 14 days after the summer solstice,
393 and the minimum DSR occurs on December 11th, 10 days before the winter solstice. We define
394 the timing of the DSR maximum and minimum relative to the solstices as RAD_{MAX} and RAD_{MIN}
395 respectively. The offset of the DSR extrema from the solstices results from the seasonal cycle of
396 atmospheric transmissivity that most likely is due to seasonal cycle in clouds (e.g. cloud fraction
397 and optical depth); this interpretation is supported by analysis of the direct versus diffuse DSR

398 which shows direct DSR is minimized on the 1st of December and is maximized on July 25th
399 (not shown) and is also consistent with the seasonality of precipitation in Seattle, which peaks in
400 November and is a minimum in late July.

401 Unlike the relationship between TOA insolation and T_{2m} at SEATAC, Fig. 5b shows that T_{2m} lags
402 DSR by a consistent phase throughout the seasonal cycle; τ_{MIN} lags RAD_{MIN} by 24 days ($14 - (-$
403 $10) = 24$ days) and τ_{MAX} lags RAD_{MAX} by 30 days ($44 - 14 = 30$ days). Thus, the seasonal phasing
404 of Seattle temperature is consistent with what is expected in a continental climate due to local
405 (1D) processes forced by DSR with seasonally invariant heat capacity and local feedbacks. Under
406 these assumptions, the temperature response lags the DSR by a constant phase across the seasonal
407 cycle – with phase determined by the ratio of the the heat capacity to the damping (Crowley and
408 North 1988). Indeed, the smoothed seasonal cycle of SEATAC temperature (green line in Fig.
409 5b) appears to lag the DSR (black line) by a fixed phase throughout the seasonal cycle. This is
410 quantified in the inset of Fig. 5b by comparing DSR (ordinate) to the temperature (abscissa) at
411 SEATAC with the latter lagged by a (seasonally invariant) time lag of 25 days; the two time series
412 are strongly correlated at $R^2 = 0.99$ indicated by a straight line (black dots in the inset of Fig. 5b).
413 In contrast the same plot of temperature versus insolation – with the optimal time lag recalculated
414 (32 days) – produces an hourglass structure (red dots) that is indicative of a time lag between
415 insolation and temperature that varies with season.

416 Seasonal variations in atmospheric shortwave transmissivity play a first order role in the season-
417 ality of DSR in Seattle; transmissivity varies by a factor of 2 from 0.3 to 0.6 between summer and
418 winter, respectively, which is smaller than – but still significant when compared to – the seasonal
419 cycle of daily mean insolation, which varies by more than a factor of 4 (between 105 and 480 W
420 m^{-2}).

421 These results motivate the following questions: How much does the seasonality of cloud cover
422 alter the seasonal timing of the DSR that drives surface temperature changes across the globe?
423 Can cloud induced shifts in the DSR extrema relative to the solstices explain the large scale pat-
424 terns of ASYM in the T_{2m} shown in Fig. 2? To answer these questions, we quantify the seasonal
425 asymmetry of DSR with the metric RAD_{ASYM} – defined to be the time of the DSR maximum
426 relative to summer solstice (RAD_{MAX}) minus the time of the DSR minimum relative to winter sol-
427 stice (RAD_{MIN}). RAD_{ASYM} can be positive or negative with positive (negative) values indicating a
428 summer maximum that is more (less) delayed than the winter minimum. For example, RAD_{ASYM}
429 has a value of $(14 - (-10)) + 24$ days for Seattle.

430 In situ DSR measurements of sufficient length to establish a global climatology of RAD_{ASYM} do
431 not exist. Thus, we calculate RAD_{ASYM} from the the satellite derived gridded climatological DSR
432 record from CERES satellite data. The CERES data from the nearest gridpoint to Seattle (blue
433 dots and lines in Fig. 5a) are in excellent agreement with the local radiometer data in absolute
434 magnitude, internal variability and, most importantly, the phasing of the seasonal cycle in DSR,
435 with RAD_{MIN} and RAD_{MAX} differing by less than 3 days between the two data sets. In the ap-
436 pendix we show that RAD_{ASYM} calculated from CERES is in close agreement with that calculated
437 using in situ DSR observations at other stations in the National Solar Radiation Database of the
438 United States of America (see Fig. A5 Sengupta et al. 2018), albeit with substantial disagree-
439 ment on the amplitude of the seasonal cycle in DSR. Specifically, station data confirm the positive
440 RAD_{ASYM} values seen in the northern latitudes of the Unites States extending from the Pacific
441 coast to the mid-west and the negative RAD_{ASYM} values seen in southwest region (influence of the
442 North America monsoon), the southeast (i.e. Florida) and in Alaska.

443 The global pattern of RAD_{MAX} (Fig. 6a) shows patterns that are regional in extent and have
444 values with magnitudes of approximately 30 days. RAD_{MAX} is positive over most of the United

445 States with largest values on the west coast. RAD_{MAX} is positive in the Mediterranean region
446 and near zero in Northern Europe. Negative values of RAD_{MAX} are seen in the monsoon regions
447 of India, South-East Asia, Africa and South-West North America where cloud cover increases
448 well before the summer solstice and is sustained thereafter, resulting in maximum DSR prior
449 to monsoon onset. Over the oceans, there is a pronounced North-South dipole of RAD_{MAX} in
450 the North Pacific, North Atlantic, South Pacific and South Atlantic with positive values on the
451 equatorward flank of the storm track and negative values on the poleward flank. The sharp north-
452 south dipole in RAD_{MAX} is a genuine feature of the data that we illustrate in the inset of Figure 6a
453 by plotting the time series of DSR at two points on different sides of dipole in the North Pacific
454 (indicated by the red and blue circles on the map). To the south of the nodal line, RAD_{MAX} occurs
455 30 days after the summer solstice (red time series) whereas to the north RAD_{MAX} occurs 30 days
456 before the summer solstice (blue time series). This dipole reflects a poleward shift of the storm
457 track from spring to summer, with reduced cloud cover prior to the shift (i.e. in the spring) on the
458 poleward side and after the shift (i.e. in the late summer) on the equatorward flank.

459 The negative values of RAD_{MAX} in the marginal ice zones, especially in the Southern Ocean,
460 reflect the retreat of sea ice prior to the summer solstice by the following mechanism: the high
461 surface albedo of the ice in the spring reflects solar radiation incident on the surface and a portion
462 of this upwelling solar radiation from the surface is reflected back to surface by clouds (Taylor
463 et al. 2007; Donohoe and Battisti 2011). The presence of ice in the spring enhances both upwelling
464 solar radiation at the surface and DSR with a net decrease in solar radiation absorbed at the surface.
465 Thus, the negative values of RAD_{MAX} in the marginal ice zones **do not** accelerate the timing of
466 τ_{MAX} since the phase advanced DSR is not indicative of the timing of *net* solar input to the surface.

467 The global pattern of the timing of the DSR minimum relative to the winter solstice (RAD_{MIN}
468 – Fig. 6b) has much smaller amplitudes than that of RAD_{MAX} . We find no obvious explanation

469 for this result. Because RAD_{MIN} is everywhere smaller in magnitude than RAD_{MAX} , RAD_{ASYM}
470 strongly resembles the map of RAD_{MAX} (c.f. Fig. 6c and a,b) .

471 We now evaluate whether the seasonal timing of DSR and temperature are correlated at the
472 global scale by comparing the spatial structure of RAD_{ASYM} (colors in Fig. 6c) and ASYM (con-
473 tours with the same colorbar). On the west coast of North America, the region of highest positive
474 ASYM values and RAD_{ASYM} are co-located over the Pacific Northwest and along the Pacific coast
475 down to the Mexican border. In these regions, T_{2m} lags DSR by ≈ 15 days throughout the sea-
476 sonal cycle – consistent with a local continental response to solar forcing. Similarly, over western
477 Europe ASYM and RAD_{ASYM} are both generally positive over the Mediterranean region and are
478 near zero to the north. This finding suggests that the seasonal cycle of cloudiness may explain the
479 contrasting ASYM between the west coast of North America and Europe by way of modifying the
480 phasing of the seasonal cycle of surface heating relative to the phasing of insolation.

481 On the global scale, however, ASYM and RAD_{ASYM} are not significantly spatially correlated.
482 This is especially true over the oceans where the strong north-south dipole in RAD_{ASYM} seemingly
483 has no impact on ASYM which is predominantly negative throughout the oceans except for posi-
484 tive values in the northwest Pacific. The spatial correlation between ASYM and RAD_{ASYM} is also
485 not significant over the global land masses considered collectively due to the lack of correlation
486 over the eastern half of Eurasia. These results suggest that while RAD_{ASYM} may offer an explana-
487 tion for the contrasting ASYM in the otherwise similar maritime climates of western Europe and
488 western North America, RAD_{ASYM} is *not* the primary cause of ASYM at the global scale. Thus,
489 we look for alternative mechanistic controls of ASYM.

490 *b. Land-ocean contrast in ASYM*

491 1) THE SEASONAL EVOLUTION OF T_{2m} OVER OCEAN AND LAND

492 The prevailing (first-order) large scale pattern of ASYM consists of negative values over the
493 ocean domain and positive values over the land domain, indicative of winter minimum tempera-
494 tures that are more delayed than summer maximum temperatures over the ocean and vice versa
495 over land. We visualize the contrasting seasonal shape of T_{2m} by co-plotting temperature data
496 from a station representative of a extratropical continental climate (Tynda in the Siberia region
497 of Russia, 55°N, 125°E, 1600 feet elevation, green line, Fig. 7a) with that of a marine climate
498 (Ocean Weather Station Papa in the North Eastern Pacific, 50°N, 145°W, purple line). For point of
499 reference, ASYM for the continental record is +12 days whereas that of the marine record is -20
500 days which are typical continental and marine ASYM values across the globe (see Fig. 2c). The
501 continental station is colder on average than the marine station (mean of -4.7°C versus 8.3°C), has
502 a much larger amplitude seasonal cycle (annual harmonic amplitude of 24.2°C versus 3.8°C) and
503 has a smaller time lag between T_{2m} and insolation (annual harmonic phase lag of 35 days versus
504 87). To easily visualize differences in the shape of the seasonal cycle in these two locations, we
505 rescale T_{2m} so that curves have the same mean vertical position and distance between temperature
506 extremes, and shift the continental record to right (more delay) by 52 days (equal to the phase
507 difference of the respective annual harmonics) so that seasonal maxima are nearly aligned (dashed
508 red line). Comparing the dashed green and solid purple lines in Fig. 7a, we see (a) T_{2m} in the
509 continental record lingers in the vicinity of the summer maximum whereas the T_{2m} in the marine
510 record is sharply peaked in summer with a **delayed and more** rapid temperature increase in the
511 spring, and (b) the winter minimum in the continental record is much more sharply peaked than
512 that in the marine record, **which cools** slowly during the late autumn and winter **compared to the**

513 land station. The substantially different temporal evolutions seen at Tynda and Ocean Station Papa
514 are typical of those in continental and marine environments, respectively.

515 2) SEASONAL EVOLUTION OF ATMOSPHERIC AND OCEANIC BOUNDARY LAYER DEPTH

516 We argue below that the ASYM contrast between land and ocean domains is due to the different
517 seasonality in the depth of the atmosphere and ocean that is greatly influenced by the surface
518 forcing – hereafter referred to as the boundary layer depth. The seasonality of boundary layer depth
519 differs between the atmosphere and ocean due to the contrasting influence surface solar heating has
520 on the stability of the two fluids: increased surface solar heating in summer (compared to winter)
521 stabilizes the ocean boundary layer causing it to thin (shoal), whereas increased surface solar
522 heating destabilizes the atmosphere over land and thus greatly deepens the atmospheric boundary
523 layer (by convection) in the summer compared to winter. The seasonality of ocean mixed layer
524 depth is amplified by the seasonal cycle in surface wind stress with reduced surface wind speed in
525 the summer resulting in further shoaling of the oceanic boundary layer (Montegut et al. 2004). The
526 lag between surface temperature and solar heating increases with increased boundary layer depth
527 because: (i) a deeper layer has a greater heat capacity (thermal inertia) which is more important
528 in the ocean and (ii) a deeper layer is coupled to advective processes away from the surface which
529 is more important in the atmosphere. Together, this causes: an earlier τ_{MAX} and delayed τ_{MIN} in
530 SST (Fig. 8b,d) resulting in a positive ASYM in SST throughout the extratropics (Fig. 8f); and
531 a delayed τ_{MAX} and an earlier τ_{MIN} in surface air temperature over land (Fig. 2a,b) and hence
532 positive ASYM (Fig. 2c).

533 The negative ASYM in SST is due to slower cooling of the SST in the winter and early spring
534 (blue time series in Fig. 9) in contrast to a rapid warming of SST in the fall. This temporal evolu-
535 tion of SST is ubiquitous in the mid-latitude oceans, is well represented in the gridded reanalysis

536 (cyan time series in Fig. 9) and, it differs substantially from an annual sinusoid. We illustrate
 537 the impact of seasonal variations in mixed layer depth on the seasonal evolution of SST using a
 538 simplified thermodynamic budget of the ocean mixed layer (Hasselmann 1976):

$$\frac{dH(t)SST'}{dt} = S'(t) - \lambda SST'. \quad (1)$$

539 In Eq. 1, SST is the ocean mixed layer temperature, $H(t)$ is the seasonally dependent heat capac-
 540 ity of the oceanic mixed layer, $S(t)$ is the solar radiation entering the ocean, λ is the sensitivity
 541 of turbulent fluxes (latent plus sensible) to surface temperature changes and primes ($'$) indicate
 542 anomalies from energetically balanced annual mean quantities. Note that we have ignored the
 543 role of the (seasonal anomalies in) oceanic heat flux convergence and the impact of atmospheric
 544 temperature changes on the downward surface heat fluxes. A sinusoidal solar forcing results in a
 545 sinusoidal SST response for a given temporally invariant value of H with amplitude (denoted by
 546 vertical brackets, $\|$):

$$\|SST\| = \|S\| / \sqrt{(H\sigma)^2 + \lambda^2}, \quad (2)$$

547 where $\frac{2\pi}{\sigma} = 365d$. The phase lag (ϕ) relative to the solar forcing increases with increasing H :

$$\phi = \text{atan}\left(\frac{\sigma H}{\lambda}\right). \quad (3)$$

548 H is much deeper in the winter than in the summer, however. Hence, one would expect the decrease
 549 in SST in the winter to be less than the increase in SST in the summer and the lag between the min-
 550 imum insolation and minimum SST (τ_{MIN}) would be greater than the lag between the maximum
 551 insolation and maximum SST (τ_{MIN}). This characteristic slowly evolving (i.e. delayed) minimum
 552 SST is seen at all OWS stations (Fig. 9 – blue lines). Numerical solutions with seasonally varying

553 H demonstrate that this expected seasonal dependence of phasing (eq. 3) and amplitude (eq. 2)
554 of SST roughly holds for reasonable choices of temporally variant H and λ and, furthermore, that
555 the slowly evolving SST minimum seen in Fig. 9 is replicated in these numerical simulations of
556 Eq. 1 (not shown).

557 We now turn the seasonal cycle of the surface air temperature (T_{2m}) overlying the ocean. In the
558 interior of the ocean basins, the seasonal evolution of T_{2m} mirrors that of SST with τ_{MAX} nearly
559 in-phase in the two fluids and τ_{MIN} within 2 weeks of one another (c.f. the red and blue time
560 series at OWS stations Echo and Papa in Fig. 9a,d). An in phase relationship between SST and
561 T_{2m} is expected for an isolated (no advection) atmospheric column coupled to an ocean since – far
562 from and land source – the atmosphere is primarily heated seasonally by the absorption of solar
563 radiation in the atmospheric column and damped by turbulent exchange with the ocean – with
564 seasonal energy storage in the atmospheric column being non-trivial but smaller in magnitude
565 (Fig. 7 of Donohoe and Battisti 2013). In such a system, the time scale of adjustment between
566 the atmosphere and the ocean is given by the atmospheric heat capacity ($\frac{C_p P_s}{g}$) divided by the
567 sensitivity of turbulent fluxes to the contrast between SST and T_{2m} ($\lambda_{SST} \approx 30 \text{ W m}^{-2} \text{ K}^{-1}$) which
568 is approximately 4 days. Thus the atmosphere and ocean adjust in concert to seasonal insolation
569 changes and is driven from the top down.

570 We now turn to the impact of seasonal variations in the atmospheric boundary layer depth on the
571 seasonal evolution of T_{2m} over land masses (the green line in Fig. 7a). During the summer, solar
572 heating of the surface destabilizes the surface atmosphere resulting in convection and an efficient
573 connection between the surface and mid-troposphere, where zonal advection of marine-influenced
574 air ameliorates the amplitude and alters the phase of T_{2m} (Stine and Huybers 2012). In contrast,
575 during the winter, the reduced surface solar heating results in net longwave cooling of the surface
576 that stabilizes the atmospheric boundary layer and effectively isolates the air in the boundary

577 layer from the influence of the air aloft. The result is a rapid cooling of the surface, nearly in
578 phase with winter solstice due to the low heat capacity of the surface and lower atmosphere.
579 The thermodynamic de-coupling between the atmospheric boundary and mid-troposphere over
580 the continents during the winter can be seen in the cross sections in Fig. 4: τ_{MIN} in the surface
581 boundary layer is distinct from that in the free troposphere. In contrast, τ_{MAX} is nearly vertically
582 homogenous throughout the atmosphere over the continents suggesting strong coupling between
583 the boundary layer and mid troposphere during the summer.

584 3) SEASONAL CYCLE OF T_{2m} AND AND SST IN THE WESTERN OCEAN BASINS

585 In contrast to the in-phase relationship between T_{2m} and SST seen in the interior of the ocean
586 basin, immediately downwind of the continents, the winter minimum in T_{2m} is almost 4K colder
587 than and precedes the minimum in SST by over a month (e.g. at Station Bravo and India –Fig.
588 9c,f). We demonstrate here that the seasonal evolution of both SST and T_{2m} in this region are pro-
589 foundly impacted by atmospheric advection off the continent and, thus, depart from the expected
590 behavior of an coupled atmospheric-oceanic column responding to seasonal changes in insolation
591 that was developed in the previous subsection.

592 Eq. 1 assumes that the seasonal cycle of SST is driven by solar radiation at the surface, damped
593 by turbulent energy fluxes (via λ_{SST}) and, ignores changes in the turbulent and downwelling long-
594 wave radiation that are *driven*, in part, by changes in the near surface atmospheric temperature.
595 This assumption fails on the western side of the North Atlantic and North Pacific ocean basins
596 where the seasonal input of energy into the ocean surface – defined as the amplitude of the sea-
597 sonal anomaly that is in phase with the insolation (see Donohoe and Battisti 2013)– is primarily
598 associated with the *atmosphere fluxing energy into (out of) the ocean* column during the warm
599 (cold) season (c.f Fig. 10a and b). This strong seasonal heating and cooling of the ocean im-

600 mediate downwind of the continents results from atmospheric advection off the continent that
601 amplifies the seasonal variations in ocean energy content: (i) cold air advection during winter pulls
602 energy out of the ocean (via turbulent energy fluxes) further cooling the SST and (ii) warm air ad-
603 vection during summer pushes (anomalous) energy into the ocean, further warming the SST. In
604 contrast, on the eastern side of the North Atlantic and Pacific and throughout the Southern Ocean,
605 the seasonal input of energy into the ocean column is dominated by solar heating of the surface.
606 The contrasting source of seasonal oceanic heating can be seen from a plot of the ratio of the sea-
607 sonal contribution of atmosphere-ocean exchange to that of solar heating (Fig. 10c) which is >1
608 on the western half of the basins and <1 on the eastern half. This ratio is an excellent predictor of
609 the seasonal amplitude of SST (shown in contours in Fig. 10c) which suggests that the amplitude
610 of seasonal variations in SST is set by seasonal variations in atmospheric advection and is largely
611 independent of (seasonal variations) in oceanic circulation. Because the seasonal atmospheric ad-
612 vection off the continent is nearly in phase with insolation, the phasing of the seasonal cycle of
613 SST is well captured by Eq. 3 with the departures from a sinusoid (and the differing values of
614 τ_{MAX} and τ_{MIN}) due to the seasonal evolution of H .

615 The dominant atmospheric energy balance on seasonal timescales over the western ocean basins
616 is between atmospheric advection and surface heat fluxes (c.f. Fig. 10d and e). In physical terms,
617 during the winter, westerly winds bring cold air from the continent that strongly cools (magnitude
618 $> 150 \text{ W m}^{-2}$ – Fig. 10e) the atmosphere over the western ocean basins. T_{2m} is 4K colder than
619 the SST with the contrast between SST and T_{2m} peaking in February (Fig. 9c,f). The cold air
620 pulls energy out of the warmer ocean via upward turbulent energy fluxes ($\approx 150 \text{ W m}^{-2}$,
621 not shown) – consistent with estimates of λ_{SST} . For regions in which the seasonal heating by
622 atmospheric advection exceeds that of heating by atmospheric solar absorption (denoted by ratios
623 > 1 in Fig. 10f), atmospheric heat flux divergence is balanced by upward turbulent energy fluxes.

624 Because the seasonal evolution of SST is more gradual (smaller in magnitude) than that of T_{2m} ,
625 the turbulent exchange is proportional to and in-phase with T_{2m} . Thus, the minimum in T_{2m} occurs
626 during the maximum in cold air advection (atmospheric heat flux divergence) which occurs in
627 January and February when the lateral gradient of T_{2m} between the ocean and land and the zonal
628 wind strength are greatest. In contrast, the SST will continue to cool until the radiative heating
629 exceeds the atmospheric energy flux divergence, which occurs approximately a month later.

630 From a Lagrangian perspective, the seasonal disequilibrium between T_{2m} and SST results from
631 air being advected to a region of substantially different SST on the timescale of atmospheric ad-
632 justment to the SST via the turbulent energy fluxes (4 days) due to the strong lateral gradient of
633 SST over the western ocean basin. The lateral SST gradient in the winter is a consequence of
634 atmospheric advection off the continent (Fig. 10c); thus, the τ_{MIN} contrast between T_{2m} and SST
635 result from atmospheric advection.

636 *c. Seasonal timing in the high latitudes*

637 ASYM is negative in the high latitudes of both hemispheres (Fig. 2c) with values of < -30 days
638 over the Arctic sea ice and the Greenland and Antarctic ice sheets. This seasonal asymmetry of
639 surface temperature results from the relatively short lag between the summer solstice and time of
640 maximum temperature ($\tau_{MAX} = 20-30$ days) typical of a continental climate with small surface
641 heat capacity, and long τ_{MIN} values (> 60 days). These regions are effectively isolated from
642 marine influence at all times of year. The relatively long delay in seasonal minimum temperature
643 results from the temporal evolution of insolation which deviates greatly from the annual harmonic
644 above the Arctic and Antarctic circle, where insolation flat lines at zero during the polar night (red
645 line in Fig. 7b). The definition of the winter solstice is fairly meaningless in these regions since
646 the minimum insolation is realized over the course of several months. We use the temperature

647 record at Greenland Summit Station (Shuman et al. 2001, 72.5°N and 38.5°W) over the time
648 period 2008-2018 to demonstrate the characteristic shape of the seasonal cycle of T_{2m} over the
649 high latitude ice sheets (black line in Fig. 7b). After a well defined peak in temperature in mid-
650 July, temperatures decrease steadily until the beginning of the polar night in November. During the
651 polar night, temperature continues to decrease slowly until just after the Sun rises again in March.
652 τ_{MIN} occurs just after the end of the polar night – timing that is analogous to the timing of the
653 minimum temperature in the diurnal cycle, which generally occurs just after sunrise because the
654 surface continues to cool until the absorbed solar radiation exceeds the emitted longwave radiation
655 (Holmes et al. 2013).

656 *d. Impact of monsoons on the seasonal cycle of temperature*

657 The onset of the Indian monsoon (around the beginning of June) heralds increased evaporative
658 cooling of the northern Indian Ocean and an increase in cloud cover and precipitation over the
659 continent, thereby reducing DSR and increasing the soil moisture available for evaporation and
660 cooling the surface (Gadgil 2003). The Indian monsoon region, along with a small section of the
661 North American monsoon, are the only regions on Earth where τ_{MAX} occurs before the summer
662 solstice. The timing of the temperature maximum relative to the onset of monsoonal precipitation
663 is analyzed from the station data in New Delhi, India which is representative of the climate in the
664 region (Fig. 7d). Temperature rapidly increases from the seasonal minimum in December until
665 the 1st of June, when the precipitation begins to ramp up (blue line). **Thereafter, the temperatures**
666 **gradually decline**

667 **The beginning of this cooling period corresponds to the onset of the Monsoon in the region**
668 **(India Meteorological Department 2019; Webster et al. 1998) which, in the climatological average,**
669 **occurs in the middle of May in Southwest India and approximately a month later in Northern India**

670 (see Fig. 3 of Krishnamurthy and Shukla 2000). The onset of the monsoon is coincident with an
671 increase in atmospheric water vapor (see Fig. 3 in Singh et al. 2004), a migration of the clouds
672 over the region (Sikka and Gadgil 1980), a reduction in surface solar radiation (Yasunari 1979)
673 and an increase in soil moisture (Nayak et al. 2018). It is the latter that is primarily responsible for
674 the cooling and the negative values of τ_{MAX} .

675 We note that we do not consider the seasonal timing of temperature in the Southeast Asian
676 monsoon in this study because this region is primarily equatorward of 25° and, thus, has a signifi-
677 cant semi-annual component of insolation, T_{2m} and precipitation (Misra and DiNapoli 2014) that
678 makes the definition of τ_{MAX} problematic.

679 5. Summary and conclusions

680 The phase and amplitude of the annual harmonic in surface temperature has been used exten-
681 sively in the existing literature to probe the underlying climate physics responsible for seasonality
682 and its changes under global warming (Santer et al. 2018; Laepple and Lohmann 2009; Dwyer
683 et al. 2012; Stine et al. 2009; Stine and Huybers 2012; Donohoe and Battisti 2013). We have
684 demonstrated that the departures of T_{2m} from the annual harmonic are substantial, vary greatly at
685 the regional scale across the globe and are well encapsulated by the metric ASYM – the seasonal
686 asymmetry in the lag between the solstices and the temperature extrema. To emphasize how dif-
687 ferent the temporal evolution of the seasonal cycle can be between different regions of the Earth,
688 we draw the reader’s attention to the panels of Fig. 7 which shows disparate but emblematic ex-
689 amples of contrasting seasonal cycles (scaled and shifted for ease of comparison). Fig. 7a shows
690 a typical maritime seasonal cycle of T_{2m} (station PAPA, with a prolonged seasonal minimum –
691 purple line) and a continental seasonal cycle of T_{2m} (Tynda, Siberia, with a prolonged seasonal
692 maximum – green line). Fig. 7c shows two maritime climates on the west coast of the continents

693 – one with a long duration warming period in North America (San Francisco, CA, USA – green
694 line) and one with a short duration warming period in Europe (Bergen, Norway – purple line). The
695 contrasting shape of the seasonal cycle in T_{2m} between San Francisco and Bergen highlights that
696 continentality is not the only control of the seasonal phasing of T_{2m} . Additional regional mecha-
697 nism of importance to the phasing of T_{2m} include the seasonality of cloud cover – specifically the
698 persistent summer stratus decks on the west coast of the United States that have no counterpart in
699 western Europe– and the seasonal contrasting seasonal migration of the storm track – whereby the
700 Pacific storm track is centered on Alaska while Bergen is stormy throughout the year.

701 We note that the substantial differences evident in the time series highlighted in Fig. 7a and
702 7c correspond to modest values of ASYM – -20 days for the maritime record, +12 days for the
703 continental record, +44 days for the North American record and -1 day for the European record).
704 These examples of contrasting seasonal shapes are not extreme cases; they are representative of
705 differences in the shape of the seasonal cycle encapsulated by the amplitude of large scale patterns
706 of ASYM seen across the globe. Some of these points have been made previously at the local
707 scale (van den Broeke 1998) and noted briefly in station data on a global scale (May et al. 1992)
708 but the present work provides a comprehensive global analysis of ASYM based in both reanal-
709 ysis and station data and extending throughout the troposphere. Much physical insight has been
710 gleaned from analysis of the phase and amplitude of the annual harmonic in T_{2m} that has provided
711 insights that are both fundamental and applicable to the long-term climate processes (i.e. climate
712 feedbacks) relevant to global warming. We hope that the analysis of ASYM presented here will
713 inspire future work probing the underlying physics that will lead to new insights relevant for large
714 scale processes at climate timescales.

715 We have identified in sections 4 and 5 several candidate mechanisms that explain the spatial
716 pattern of ASYM seen in various locations including: the atmospheric versus oceanic contrast in

717 seasonal boundary layer depth in response to solar heating, the phase differences in surface solar
718 radiation and top of atmosphere insolation due to clouds, and the impact of seasonal evolving
719 atmospheric circulations such as the monsoon and stationary waves. This list is by no means
720 exhaustive and we find no single mechanism that adequately explains the broad scale features of
721 ASYM.

722 We emphasize that much of our analysis is exploratory and that no one mechanism is found to
723 explain the spatial pattern of ASYM across the globe. We hope our analysis will inspire future
724 work in observational data sets and modeling (both ideal and comprehensive). For example, should
725 ASYM be realistically simulated in comprehensive models, then the representation of ASYM in
726 a hierarchy of lower complexity models (i.e. uncoupled, slab ocean, simplified radiative code,
727 single column models) would prove useful for isolating the fundamental processes responsible
728 for ASYM (and its spatial variability). An observational pathway forward would be to analyze
729 whether the phasing of the diurnal cycle varies seasonally in the same sense of ASYM. This result
730 would suggest that single column energetics associated with the atmospheric depth over which
731 surface heating is communicated is an essential component in determining ASYM (and its spatial
732 variability).

733 *Acknowledgments.* We thank Duo Chan for providing Ocean Weather Ship data and Robert Hahn
734 and Dennis D'Amico for assistance with Camp Muir temperature data. AD's work was partially
735 funded by the NSF Antarctic Program Grant Number PLR 1643436.

736 APPENDIX

737 The appendix consists of four supplemental figures to support the findings of the main text.
738 Fig. A1 show a global comparison of ASYM calculated from station data (abscissa) versus that
739 calculated from the nearest-neighbor ERA reanalysis. Fig. A2 shows the same analysis of the

740 seasonal timing of T_{2m} presented in Fig. 2 using the NCEP reanalysis 2 meter air temperature
741 instead of the ERA-interim data. Fig. A3 compares the seasonal cycle of T_{2m} at various altitudes
742 in the Seattle area using high elevation weather stations on Mount Rainier to probe the strong
743 vertical gradients in τ_{MIN}) seen in Figs. 3 and 4.

744 In Fig. A4 we present an explanation for the curious sharp west-east gradient in τ_{MIN} over the
745 ocean south of Australia in both reanalysis products (Fig. 2 and A2); τ_{MIN} values to the west
746 of Australia are typically > 70 days while those to the east are ≈ 20 days. This is an artifact,
747 however. Throughout the region there is a 100 day period where temperature is very close to the
748 seasonal minimum with a slight warming ($\approx 0.1K$) in the middle of this period (see Fig. A4)
749 resulting in two local temporal minima of T_{2m} at locations throughout the region. East (west) of
750 Australia, the absolute minimum temperature occurs early (late) in this 100 day interval. (The
751 minor local maxima in the middle of this 100 day interval is likely due to seasonal variations in
752 upwelling). We view this spatial discontinuity of τ_{MIN} as a shortcoming of the methodology used
753 here to characterize the seasonal cycle of T_{2m} which was intended to represent a seasonal cycle
754 with only one maximum and minimum.

755 References

- 756 Barnes, E., and I. Simpson, 2017: Seasonal sensitivity of the northern hemisphere jet streams to
757 arctic temperatures on subseasonal time scales. *J. Climate*, **30**, 10 117–10 137.
- 758 Belka, D., M. Schwendeman, J. Thomson, and M. Cronin, 2014: Historical wave and wind obser-
759 vations at Ocean Station P. *APL Technical Report*.
- 760 Berger, A., 1978: Long-term variations of caloric insolation resulting from Earth’s orbital element.
761 *Quaternary Res.*, **9**, 139–167.

- 762 Brooks, C., 1917: Continentiality and temperature. *Quat. J. Met. Soc.*, **43**, 159–174.
- 763 Crowley, T., and G. North, 1988: Abrupt climate change and extinction events in Earth history.
764 *Science*, **240 (996)**, 1002.
- 765 D’Amico, D., 2019: Camp Muir weather data. *Northwest Avalanche Center Technical Report*.
- 766 Dee, D., and Coauthors, 2011: The ERA-Interim reanalysis: Configuration and perfor-
767 mance of the data assimilation system. *Quat. J. Met. Soc.*, **137**, 553–597, URL <https://www.ecmwf.int/en/forecasts/datasets/reanalysis-datasets/era-interim>, [accessed 05-January-
768 //www.ecmwf.int/en/forecasts/datasets/reanalysis-datasets/era-interim, [accessed 05-January-
769 2018, <https://www.ecmwf.int/en/forecasts/datasets/reanalysis-datasets/era-interim>].
- 770 Donohoe, A., and D. Battisti, 2011: Atmospheric and surface contributions to planetary albedo. *J.*
771 *Climate*, **24 (16)**, 4401–4417.
- 772 Donohoe, A., and D. Battisti, 2013: The seasonal cycle of atmospheric heating and temperature.
773 *J. Climate*, **26 (14)**, 4962–4980.
- 774 Donohoe, A., D. Frierson, and D. Battisti, 2013: The effect of ocean mixed layer depth on
775 climate in slab ocean aquaplanet experiments. *Climate Dyn.*, **26**, 15 Pages, doi:10.1007/
776 s00382-013-1843-4.
- 777 Downes, C., 1977: History of the British ocean weather ships. *The Marine Observer*, **XLVII**,
778 179–186.
- 779 Dwyer, J., M. Biasutti, and A. Sobel, 2012: Projected changes in the seasonal cycle of surface
780 temperature. *J. Climate*, **25**, 6359–6374.
- 781 Eliassen, A., and E. Palm, 1961: On the transfer of energy in stationary mountain waves. *Geof.*
782 *Pub.*, **22 (5)**, 1–23.

- 783 Gadgil, S., 2003: The Indian monsoon and its variability. *Annu. Rev. Earth Planet. Sci.*, **31**, 429–
784 467.
- 785 Hasselmann, K., 1976: Stochastic climate models. *Tellus*, **28**, 473–485.
- 786 Held, I., 2001: Northern winter stationary waves: theory and modeling. *J. Climate*, **15**, 2125.
- 787 Holmes, T., W. Crow, and C. Hain, 2013: Spatial patterns in the timing of the diurnal temperature
788 cycle. *Hydro. Earth Sys. Sci.*, **17**, 3695–3706.
- 789 Hurley, J., and W. Boos, 2015: A global climatology of monsoon low-pressure systems. *Quat. J.*
790 *Met. Soc.*, **141 (680)**, 1049–1064.
- 791 India Meteorological Department, 2019: Accessed: 2019-08-30, [http://www.imd.gov.in/pages/
792 monsoon_main.php](http://www.imd.gov.in/pages/monsoon_main.php).
- 793 Kato, S., and Coauthors, 2018: Surface irradiances of edition 4.0 clouds and the Earth’s radiant
794 energy system (CERES) energy balanced and filled (EBAF) data product. *J. Climate*, **31 (11)**,
795 4501–4527.
- 796 Krishnamurthy, V., and J. Shukla, 2000: Intraseasonal and interannual variability of rainfall over
797 india. *J. Climate*, **13**, 4366–4377.
- 798 Laepple, T., and G. Lohmann, 2009: Seasonal cycle as a template for climate variability
799 on astronomical timescales. *Paleoceanography and Paleoclimatology*, **24 (4)**, doi:10.1029/
800 2008PA001674.
- 801 Loeb, N. G., and Coauthors, 2018: Clouds and the Earth’s radiant energy system (CERES) en-
802 ergy balanced and filled (EBAF) top-of-atmosphere (TOA) edition 4.0 data product. *J. Climate*,
803 **31 (2)**, 895–918.

804 May, W., D. Shea, and C. Madden, 1992: The annual variation of surface temperature over the
805 world. *NCAR Tech. Note*, NCAR/TN-372+STR.

806 McKinnon, K., A. Stine, and P. Huybers, 2013: The spatial structure of the annual cycle in surface
807 temperature: amplitude, phase and Lagrangian history. **26**, 7852–7862.

808 Misra, V., and S. DiNapoli, 2014: The variability of the southeast Asian summer monsoon. *Int. J.*
809 *Climatol.*, **34**, 893–901.

810 Montegut, C., G. Madec, A. Fischer, A. Lazar, and D. Ludicone, 2004: Mixed layer depth over the
811 global ocean; An examination of profile data and profile-based climatology. *J. Geophys. Res.*,
812 **19 (C12003)**, doi:10.1029/2004JC002378.

813 Nayak, H., K. Osuri, P. Sinha, R. Nadimpalli, U. Mohanty, F. Chen, M. Rajeevan, and D. Niyogi,
814 2018: High-resolution gridded soil moisture and soil temperature datasets for the Indian mon-
815 soon region. *Scientific Data*, **5**, 180 264.

816 North, G. R., and J. A. Coakley, 1978: Simple seasonal climate models. *Meteorol. Gidrol.*, **5**,
817 26–32.

818 Peixoto, J., and A. Oort, 1992: *Physics of Climate*. AIP Press, 160 pp pp.

819 Peterson, T., and R. Vose, 1997: An overview of the global historical cli-
820 matology network temperature database. *Bull. Amer. Meteor. Soc.*, **78 (12)**,
821 2837–2840, URL [https://www.ncdc.noaa.gov/data-access/land-based-station-data/
822 land-based-datasets/global-historical-climatology-network-ghcn](https://www.ncdc.noaa.gov/data-access/land-based-station-data/land-based-datasets/global-historical-climatology-network-ghcn), [Accessed 14-October-2017,
823 [https://www.ncdc.noaa.gov/data-access/land-based-station-data/land-based-datasets/global-
824 historical-climatology-network-ghcn](https://www.ncdc.noaa.gov/data-access/land-based-station-data/land-based-datasets/global-historical-climatology-network-ghcn)].

- 825 Prescott, J., and J. Collins, 1948: The lag of temperature behind solar radiation. *Quat. J. Met. Soc.*,
826 **77**, doi:121-126.
- 827 Reynolds, R., T. Smith, C. Liu, D. Chelton, K. Casey, and M. Schlax, 2007: Daily high-resolution-
828 blended analyses for sea surface temperature. *J. Climate*, **20**, 5473–5496, URL [https://www.esrl.](https://www.esrl.noaa.gov/psd/data/gridded/data.noaa.oisst.v2.highres.html#detail)
829 [noaa.gov/psd/data/gridded/data.noaa.oisst.v2.highres.html#detail](https://www.esrl.noaa.gov/psd/data/gridded/data.noaa.oisst.v2.highres.html#detail), [Accessed 24-March-2018,
830 <https://www.esrl.noaa.gov/psd/data/gridded/data.noaa.oisst.v2.highres.html>].
- 831 Santer, B., S. Po-Chedley, M. Zelinka, I. Cvijanovic, C. Bonfils, and P. Durack, 2018: Human
832 influence on the seasonal cycle of tropospheric temperature. *Science*, **361 (6399)**, doi:10.1126/
833 [science.aas8806](https://doi.org/10.1126/science.aas8806).
- 834 Sengupta, M., Y. Xie, A. Lopez, A. Habtea, G. Maclaurin, and J. Shelby, 2018: The national solar
835 radiation data base (NSRDB). *Renew. Sust. Energ. Rev.*, **89**, 51–60.
- 836 Sheridan Dodds, P. L. M., A. Reagan, and C. Danforth, 2016: Tracking climate change through
837 the spatiotemporal dynamics of the teletherms, the statistically hottest and coldest days of the
838 year. *Plos One*, doi:10.1371/journal.pone.0154184.
- 839 Shuman, C., K. Steffen, and J. Box, 2001: A dozen years of temperature observations at the
840 summit: Central greenland automatic weather stations 1987-99. *J. Adv. Model. Earth Sy.*, **40**,
841 741–753.
- 842 Sikka, D., and S. Gadgil, 1980: On the maximum cloud zone and the ITCZ over Indian longitudes
843 during the southwest monsoon. *Mon. Weath. Rev.*, **108**, 1840–1853.
- 844 Singh, R., S. Dey, S. Tripathi, and V. Tare, 2004: Variability of aerosol parameters over Kanpur,
845 Northern India. *J. Geophys. Res.*, **109**, doi:10.1029/2004JD004966.

846 Stine, A., and P. Huybers, 2012: Changes in the seasonal cycle of temperature and atmospheric
847 circulation. *J. Climate*, **25**, 7362–7380.

848 Stine, A., P. Huybers, and I. Fung, 2009: Changes in the phase of the annual cycle of surface
849 temperature. *Nature*, **457 (435- 440)**, 123–139.

850 Taylor, K., M. Crucifix, P. Braconnot, C. Hewitt, C. Doutriaux, A. Broccoli, J. Mitchell, and
851 M. Webb, 2007: Estimating shortwave radiative forcing and response in climate models. *J.*
852 *Climate*, **20**, 2530–2543.

853 Thomson, D., 1995: The seasons, global temperature, and precession. *Science*, **268**, 59–68.

854 Trenberth, K. E., 1991: Storm tracks in the Southern Hemisphere. *J. Atmos. Sci.*, **48**, 2159–2178.

855 US Weather Bureau, 1977: Changes made in ocean projects. *Weather Bureau Topics*, **10**, 132.

856 van den Broeke, M., 1998: The semi-annual oscillation and antarctic climate. Part 1: Influence on
857 near surface temperatures (1957-79). *Antarct. Sci.*, **10**, 175–183.

858 Von Hann, J., and R. Ward, 1903: *Handbook of Climatology*. MacMilan.

859 Wallace, C., and T. Osborn, 2002: Recent and future modulation of the annual cycle. *Clim. Res.*,
860 **222**, 1–11.

861 Webster, P., V. Magan, T. Palmer, J. Shukla, R. Tomas, M. Yanai, and T. Yasunari, 1998: Mon-
862 soons: Processes, predictability, and the prospects of prediction. *J. Geophys. Res.*, **103 (C7)**,
863 104451–14510.

864 World Meteorological Organization, 2011: Guide to climatological practices. 117 Pages.

865 Yasunari, T., 1979: Cloudiness fluctuations associated with the northern hemisphere summer mon-
866 soon. *J. Meteor. Soc. Japan*, **57**, 227–242.

867 **LIST OF FIGURES**

868 **Fig. 1.** (Top Panel) Seasonal cycle of daily average surface (2m air) temperature (T_{2m}) at SEATAC
 869 airport on a partially repeated periodic domain. The dots show daily data for individual
 870 years. The black thin lines show the climatological average for each calendar day and the
 871 thick black line shows the spline fit to the data. The vertical black lines show the date of
 872 the spline fit maximum (τ_{MAX}) and minimum (τ_{MIN}) and the vertical red line shows the date
 873 of summer and winter solstices. The dashed blue line shows the annual harmonic fit. Ticks
 874 on the x-axis are on the start of each calendar month. (Bottom Panel) As in the top panel
 875 but superimposed with T_{2m} taken from with the nearest grid point to SEATAC in the ERA-
 876 Interim reanalysis product. The light blue shaded area represents the one standard deviation
 877 of the ERA data. The solid blue line is the spline fit to the ERA data and vertical blue lines
 878 show the date of the τ_{MAX} and τ_{MIN} . **The monthly ticks along the abscissa indicate the first**
 879 **day of the month here and elsewhere in this paper** 43

880 **Fig. 2.** (a) Time lag of maximum temperature relative to the summer solstice (τ_{MAX}). Colors show
 881 results from the gridded ERA surface temperature data and the individual dots show the
 882 location of the station data color coded by the time lag given by the common colorbar in
 883 the upper right. (b) As in (a), **but** for the time lag of the minimum temperature relative to
 884 the winter solstice (τ_{MIN}). (c) The asymmetry (ASYM) in the timing of the seasons defined
 885 as the top panel minus the middle panel. This panel uses the colorbar on the lower right.
 886 The spatial correlation (**R**) between values at all stations and that at the nearest gridpoint is
 887 shown in the middle of each plot **along with the mean absolute difference**. 44

888 **Fig. 3.** Vertical structure of the seasonal timing of **atmospheric temperature at various pressure lev-**
 889 **els** in the ERA reanalysis. Time lag of the seasonal maximum temperature (τ_{MAX} , left col-
 890 umn), minimum temperature (τ_{MIN} , left column) and, timing asymmetry (ASYM, right col-
 891 umn) defined as the left column minus the right column. Each row is a different pressure
 892 level with the surface (repeated from Fig. 2) at the bottom to 800, 600 and, 400 hPa (top
 893 row). 45

894 **Fig. 4.** Longitude/altitude cross sections of seasonal timing averaged between **47°N and 57°N**. (a)
 895 The time lag of the seasonal maximum relative to the summer solstice; (b) the time lag of
 896 the seasonal minimum relative to the winter solstice; and (c) shows the seasonal asymmetry
 897 in the timing defined as the difference between (a) and (b). The contours show the results
 898 from the ERA reanalysis with contour interval 10 days with color values shown in the color
 899 bar (zero contour in gray). The color filled circles show results from surface stations and
 900 Ocean Weather Ships (jittered about 1000 hPa for visual purposes) and the dots at higher
 901 elevations show the high altitude stations on Mt. Rainier, WA, USA. 46

902 **Fig. 5.** (a) Seasonal time series of the downwelling surface solar radiation (black) measured at the
 903 University of Washington (UW ATG), Seattle and at (blue) the nearest gridpoint of the
 904 CERES data. Black dots show the individual daily mean values at UW ATG, the thin black
 905 line is the climatological mean for the calendar day and the thick black line is the spline
 906 fit. The shaded blue area is bounded by the maximum and minimum CERES values for the
 907 calendar day over the record (**2000-2018**), the thin blue line is the climatological mean for
 908 the calendar day and the thick blue line is the spline fit. The red line shows the (top of atmo-
 909 sphere downward) insolation from CERES. Vertical black and blue lines show the timing of
 910 the (spline fit) maximum and minimum surface solar radiation in the CERES and UW ATG
 911 data respectively and the vertical red lines show the summer and winter solstice. (b). Sea-
 912 sonal time series of the spline fit (black) UW ATG surface solar radiation and (green) T_{2m}
 913 at SEATAC. The inset shows the relationship between T_{2m} at SEATAC and (black) surface

| | | |
|-----|---|----|
| 914 | solar radiation at an optimal lead of 25 days and (red) top of atmosphere insolation at an | |
| 915 | optimal lead of 32 days. | 47 |
| 916 | Fig. 6. (a) Timing of maximum in surface solar radiation relative to the summer solstice from the | |
| 917 | CERES dataset. (b) Timing of seasonal minimum of surface solar radiation relative to the | |
| 918 | winter solstice. (c) Seasonal asymmetry of surface solar radiation defined as the difference | |
| 919 | between the top and middle panel. The contours show the seasonal asymmetry of surface | |
| 920 | temperature (ASYM) from the ERA surface data (repeated from Figure 3) with contour | |
| 921 | interval of 10 days using the same colorbar as the surface solar timing (zero contour is | |
| 922 | omitted). In panel (a), the inset shows the time series of downwelling surface solar radiation | |
| 923 | at two gridpoints straddling the strong north-south gradient in the North Pacific (marked by | |
| 924 | circles on the map) with timing of the maximum shown by the vertical lines. | 48 |
| 925 | Fig. 7. (a) Comparison of the seasonal cycle of surface temperature at a typical continental location | |
| 926 | (Tynda, Siberia – green) and a maritime location (Weather Station Papa – purple). The | |
| 927 | maritime record has been rescaled by a factor of 6 (c.f. the left, green and right, purple | |
| 928 | y-axes) so that the seasonal cycles are visible on the same axis. Dots show the daily data and | |
| 929 | the lines show the spline fit to the data; vertical lines show the timing of the extrema. The | |
| 930 | dashed green line shows the continental record lagged by 42 days (such that the maximum | |
| 931 | are in phase) to highlight the different shapes of the seasonal cycle over land and ocean. | |
| 932 | (b) Seasonal times series of temperature (black) and solar radiation at the surface (dashed | |
| 933 | red) and insolation at TOA (solid red) at Greenland Summit Station. (c) As in panel B | |
| 934 | except a comparison on maritime climates in western North America (San Francisco airport, | |
| 935 | USA, green) and western Europe (Bergen, Norway, purple). (d) Seasonal time series of | |
| 936 | temperature (black) and precipitation (blue) at New Delhi, India. | 49 |
| 937 | Fig. 8. Comparison of seasonal timing of T_{2m} and SST over the oceans. The left panels show τ_{MAX} , | |
| 938 | τ_{MIN} and ASYM defined from surface air temperature (from ERA 1000 hPa) and the right | |
| 939 | panels show the same quantities calculated from SST data (NOAA OISST). The dots show | |
| 940 | the ocean weather ship locations and are color coded by the timing of the station measured | |
| 941 | T_{2m} in the left panel and SST in the right panel. | 50 |
| 942 | Fig. 9. (a,c,d,f) Time series of smoothed seasonal cycles of (blue) SST and (red) surface air tem- | |
| 943 | perature (T_{2m}) at selected OWS locations. The cyan line shows the NOAA OISST data and the nearest neighbor gridpoint. The orange line shows the ERA reanalysis T_{2m} data at the nearest neighbor gridpoint. The stations are organized by those with negative (positive) ASYM in T_{2m} on the left (right) and those where the timing is well (poorly) replicated in the gridded data on the top (bottom). The maps of ASYM defined from the SST data (NOAA OISST) and the ERA surface air temperature data respectively (previously shown in Fig. 8) are shown in panels b and e with the highlighted stations labeled by the letter of the panel they appear in (just above the station location) to orient the reader. | 51 |
| 951 | Fig. 10. The source of seasonal heating of the (top) ocean and (bottom) atmosphere defined as the | |
| 952 | seasonal amplitude of energy input phase with the insolation. The oceanic energy input is | |
| 953 | broken down into (a) surface solar radiation and (b) energy exchange with the atmosphere. | |
| 954 | Panel (c) shows the ration (atmospheric exchange divided by solar heating); the seasonal | |
| 955 | amplitude of SST is overlaid in contours. The atmospheric energy input is broken down | |
| 956 | into (d) solar radiation absorbed in the atmospheric column and (e) atmospheric energy flux | |
| 957 | convergence (advection). Panel (f) shows the ratio (advection to solar); the phase advance | |
| 958 | of the atmospheric minimum temperature relative to the SST minimum is shown in green | |
| 959 | contours. | 52 |

960 **Fig. A1.** Scatter plot of (ordinate) ASYM calculated from the station data versus (abscissa) the
961 ASYM calculated from the ERA surface temperature at the nearest grid point. The dashed
962 black line is the 1:1 line and the red line is the linear best fit. 53

963 **Fig. A2.** As in Fig. 2 except for the NCEP reanalysis. (a) Time lag of seasonal maximum temperature
964 relative to the summer solstice. Colors show results from the gridded 2 meter air temperature
965 from the NCEP reanalysis and the individual dots show the location of the station data color
966 coded by the time lag given by the common colorbar to the right. (b) As in (A) except for
967 the time lag of the minimum temperature relative to the winter solstice. (c) The asymmetry
968 in the timing of the seasons (ASYM), defined as (a) minus (b). This panel uses the colorbar
969 on the lower right. 54

970 **Fig. A3.** Comparison of seasonal cycle of temperature on Mount Rainier at (red) Paradise (elevation
971 5,400 feet) and (blue) Camp Muir (elevation 10,188 feet) with that near sea level at (black)
972 SEATAC. The gray dashed line is the seasonal cycle of SST at ocean station PAPA shifted
973 and rescaled for visual comparison. The vertical lines indicate the timing of τ_{MAX} and τ_{MIN}
974 in each time series given by the same color. 55

975 **Fig. A4.** Time series of ERA surface air temperature at gridpoints separated by 3° longitude spanning
976 the discontinuity in ASYM south of Australia seen in Fig. 2c at 55°S . The blue time series
977 is from 55^{circ}S , 145°E with ASYM = -44 days and the red time series is from 55°S , 148°E
978 with ASYM = +27 days. The dashed vertical lines show the timing of τ_{MIN} and τ_{MAX} for
979 the time series of the same color. 56

980 **Fig. A5.** Comparison of RAD_{MAX} , RAD_{MIN} and RAD_{ASYM} calculated in the gridded CERES data to
981 that calculated using DSR measurements from the US (Sengupta et al. 2018). The dots show
982 the observed daily mean DSR and the solid lines show the smoothed climatological seasonal
983 cycle. The direct radiation is shown in red, the diffuse in green and the total observed DSR in
984 black. The dashed black line shows the smoothed seasonal cycle of total DSR from CERES
985 data at the nearest neighbor gridbox. Vertical lines show the time of RAD_{MAX} and RAD_{MIN}
986 identified in the smoothed timeseries of the same linetype. The purple vertical lines show
987 the winter and summer solstices. The inset map shows the RAD_{ASYM} values at each of the
988 stations (colored dots circumscribed by gray) overlaid on (colors) RAD_{ASYM} calculated
989 from the CERES DSR data. 57

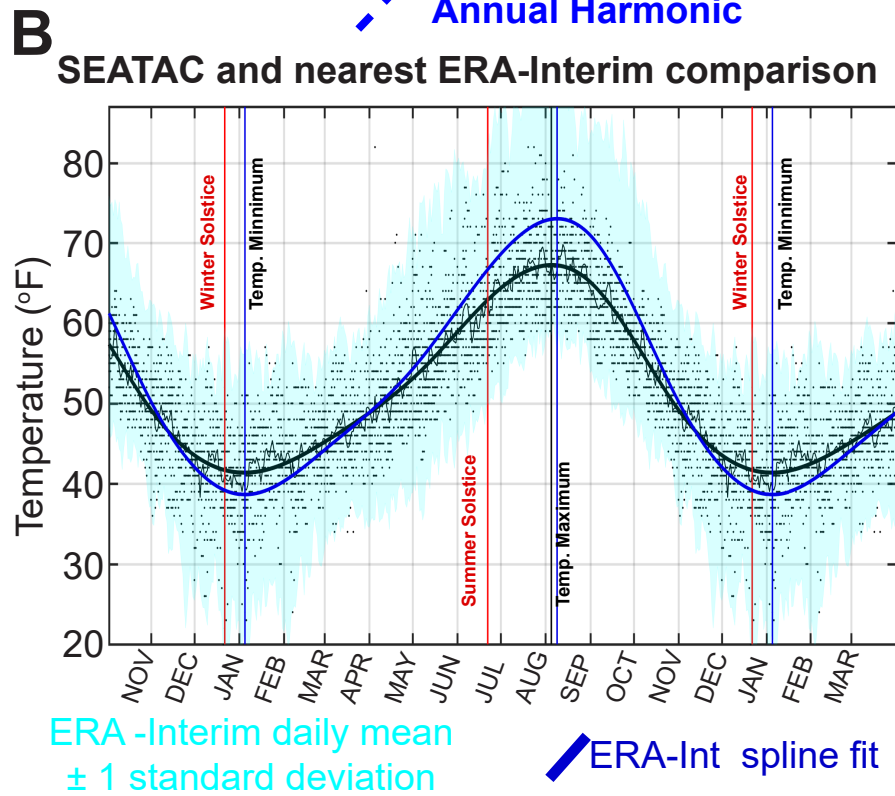
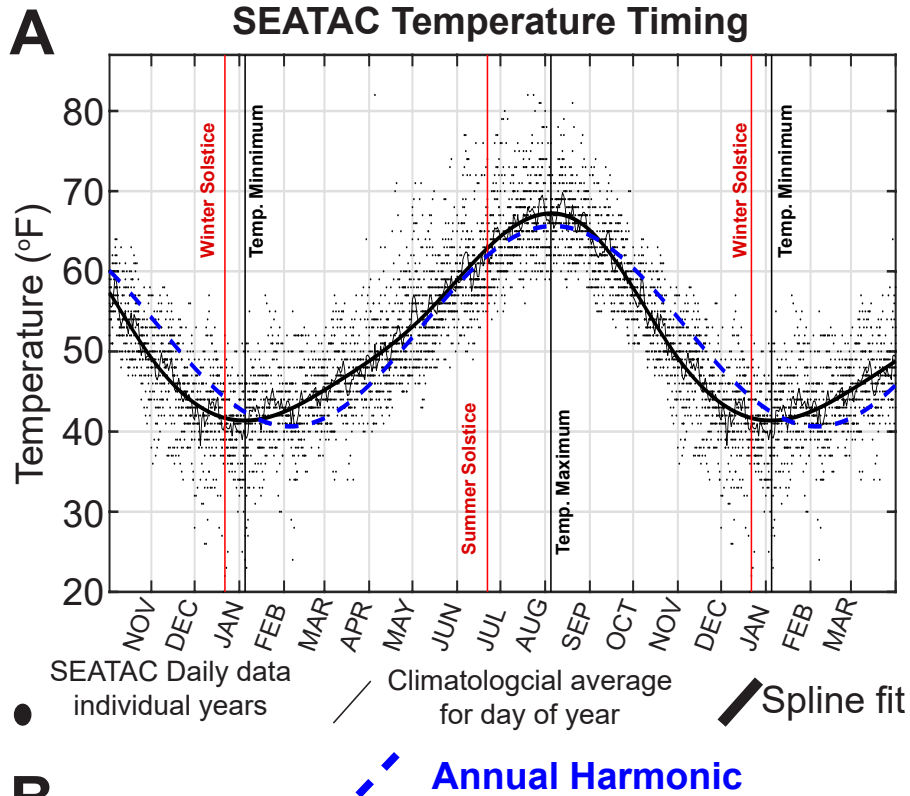
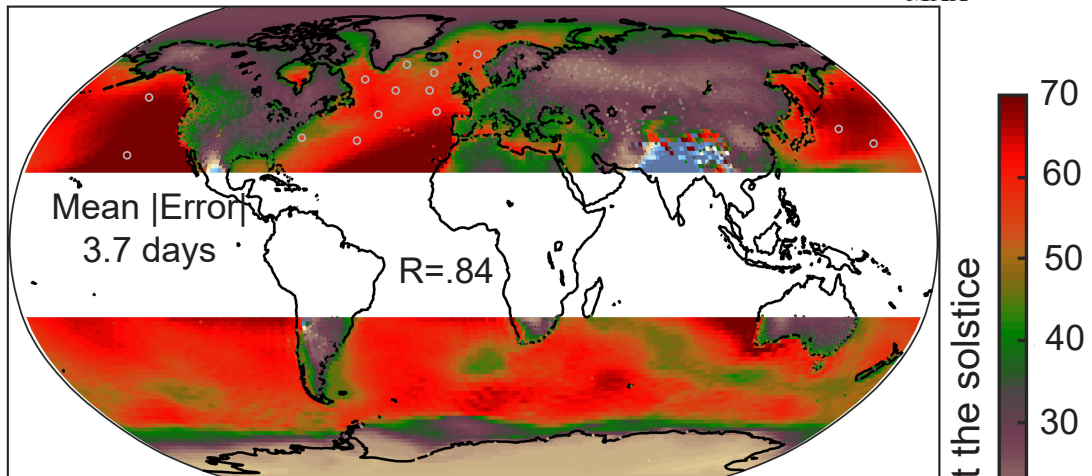
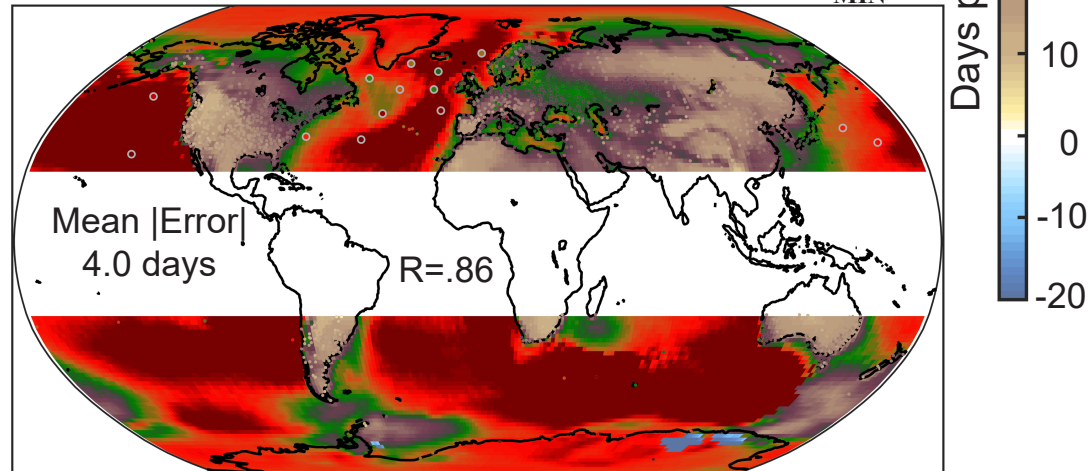


FIG. 1: (Top Panel) Seasonal cycle of daily average surface (2m air) temperature (T_{2m}) at SEATAC airport on a partially repeated periodic domain. The dots show daily data for individual years. The black thin lines show the climatological average for each calendar day and the thick black line shows the spline fit to the data. The vertical black lines show the date of the spline fit maximum (τ_{MAX}) and minimum (τ_{MIN}) and the vertical red line shows the date of summer and winter solstices. The dashed blue line shows the annual harmonic fit. Ticks on the x-axis are on the start of each calendar month. (Bottom Panel) As in the top panel but superimposed with T_{2m} taken from with the nearest grid point to SEATAC in the ERA-Interim reanalysis product. The light blue shaded area represents the one standard deviation of the ERA data. The solid blue line is the spline fit to the ERA data and vertical blue lines show the date of the τ_{MAX} and τ_{MIN} . The monthly ticks along the abscissa indicate the first day of the month here and elsewhere in this paper.

A Time lag of maximum temperature-- τ_{MAX}



B Time lag of minimum temperature-- τ_{MIN}



C Asymmetry of Seasonal Time lag (A-B)

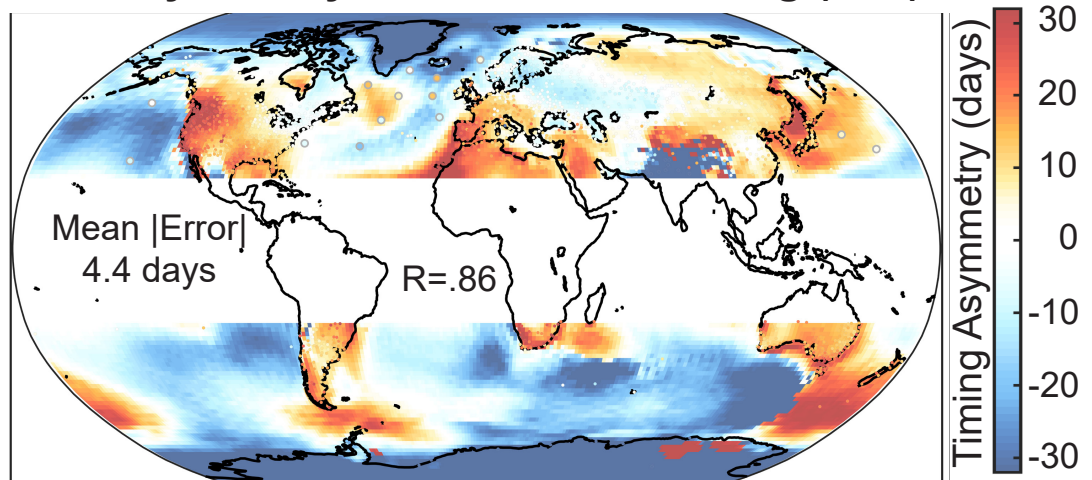


FIG. 2: (a) Time lag of maximum temperature relative to the summer solstice (τ_{MAX}). Colors show results from the gridded ERA surface temperature data and the individual dots show the location of the station data color coded by the time lag given by the common colorbar in the upper right. (b) As in (a), but for the time lag of the minimum temperature relative to the winter solstice (τ_{MIN}). (c) The asymmetry (ASYM) in the timing of the seasons defined as the top panel minus the middle panel. This panel uses the colorbar on the lower right. The spatial correlation (R) between values at all stations and that at the nearest gridpoint is shown in the middle of each plot along with the mean absolute difference.

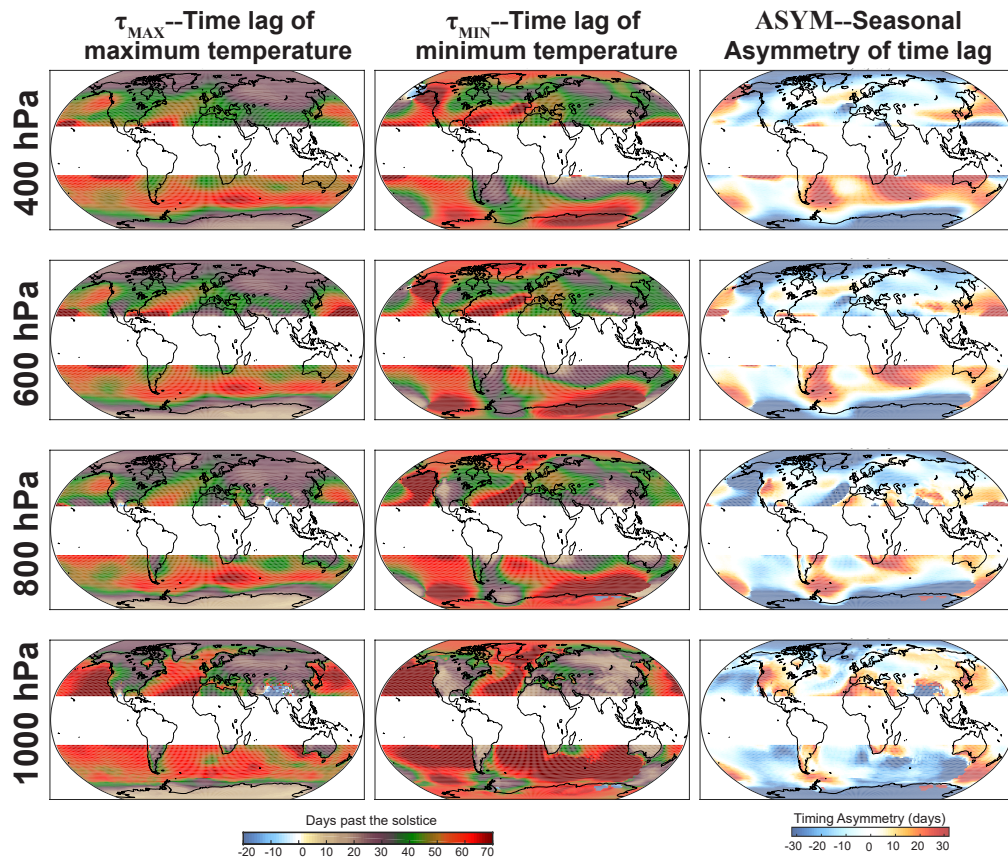


FIG. 3: Vertical structure of the seasonal timing of atmospheric temperature at various pressure levels in the ERA reanalysis. Time lag of the seasonal maximum temperature (τ_{MAX} , left column), minimum temperature (τ_{MIN} , left column) and, timing asymmetry (ASYM, right column) defined as the left column minus the right column. Each row is a different pressure level with the surface (repeated from Fig. 2) at the bottom to 800, 600 and, 400 hPa (top row).

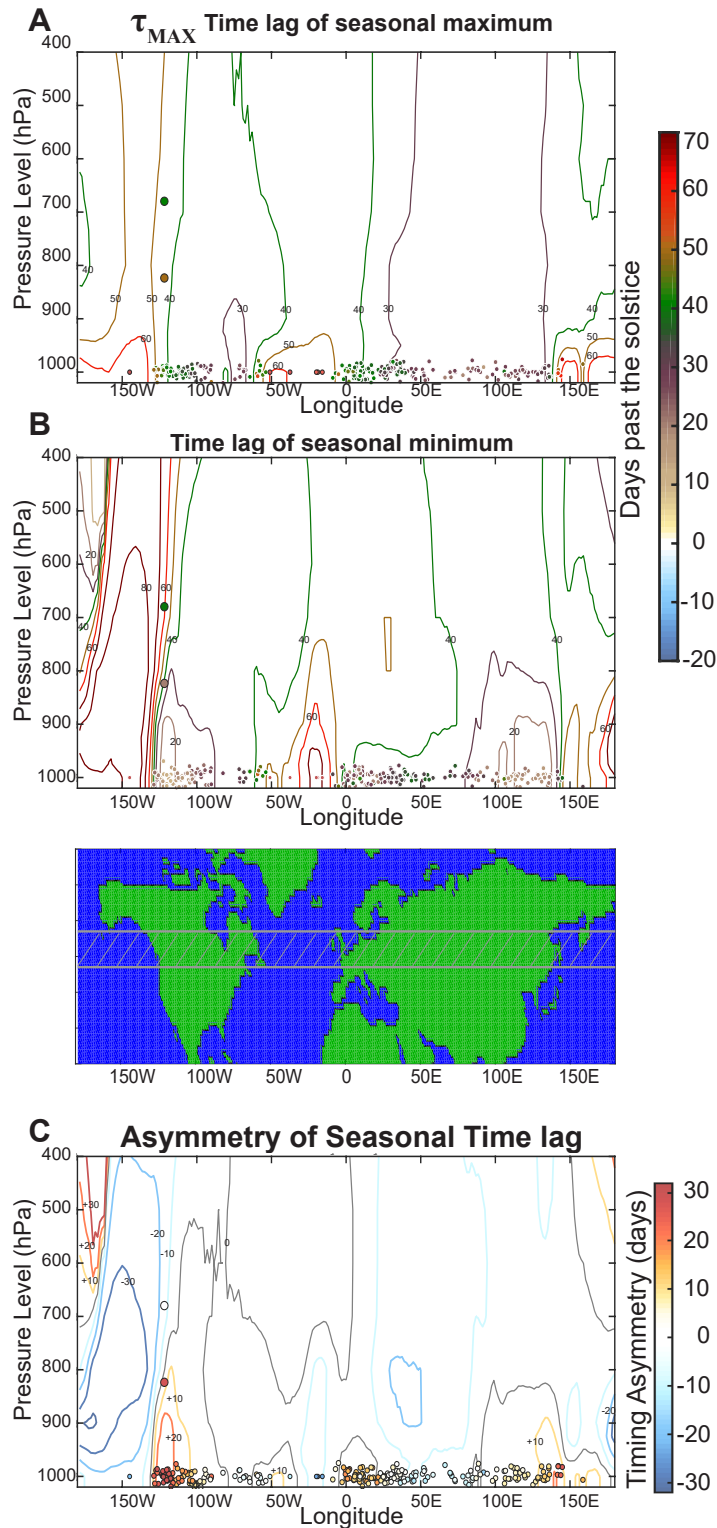


FIG. 4: Longitude/altitude cross sections of seasonal timing averaged between 47°N and 57°N . (a) The time lag of the seasonal maximum relative to the summer solstice; (b) the time lag of the seasonal minimum relative to the winter solstice; and (c) shows the seasonal asymmetry in the timing defined as the difference between (a) and (b). The contours show the results from the ERA reanalysis with contour interval 10 days with color values shown in the color bar (zero contour in gray). The color filled circles show results from surface stations and Ocean Weather Ships (jittered about 1000 hPa for visual purposes) and the dots at higher elevations show the high altitude stations on Mt. Rainier, WA, USA.

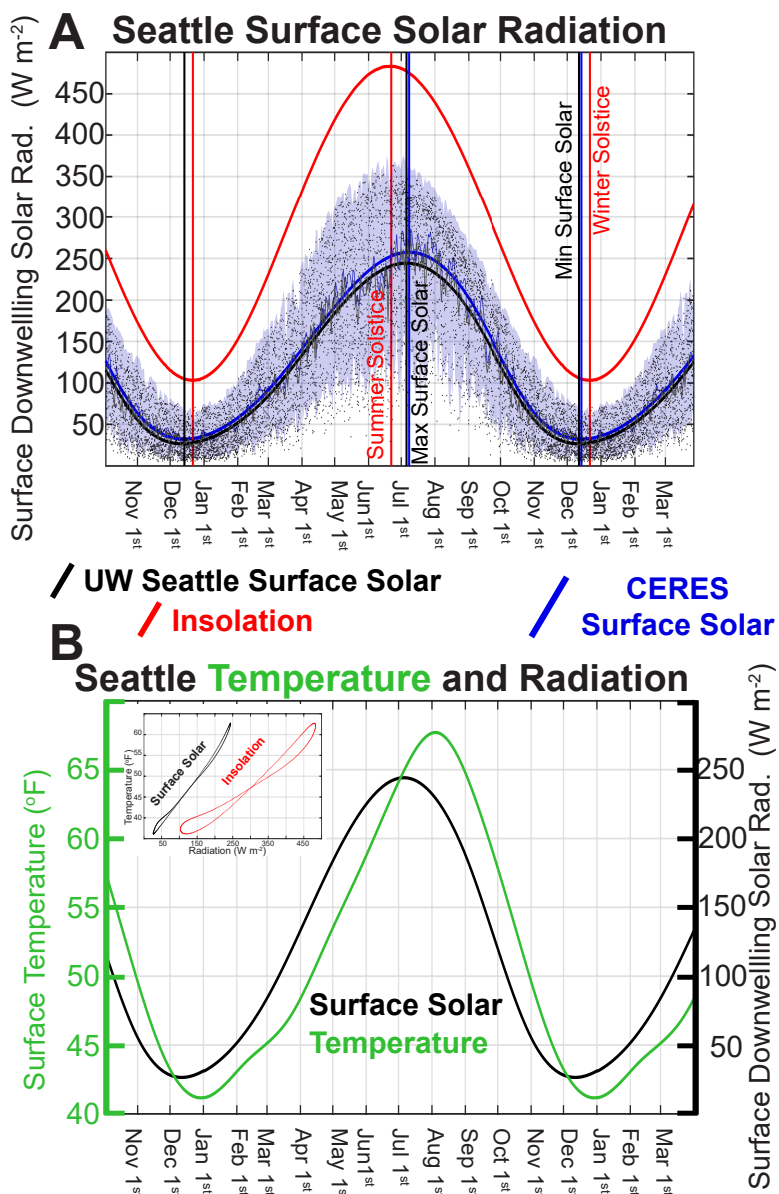
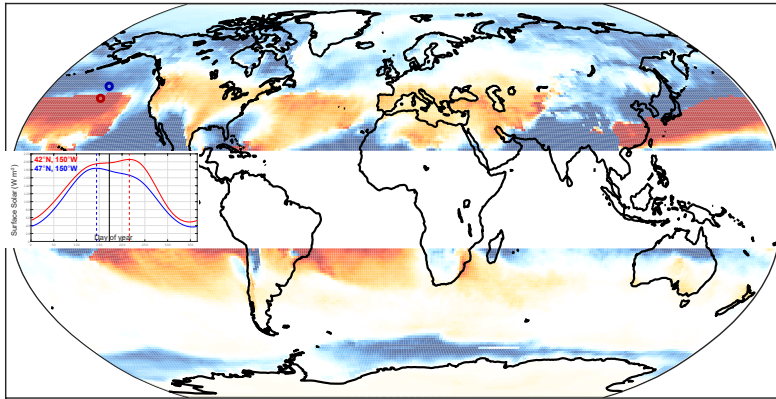
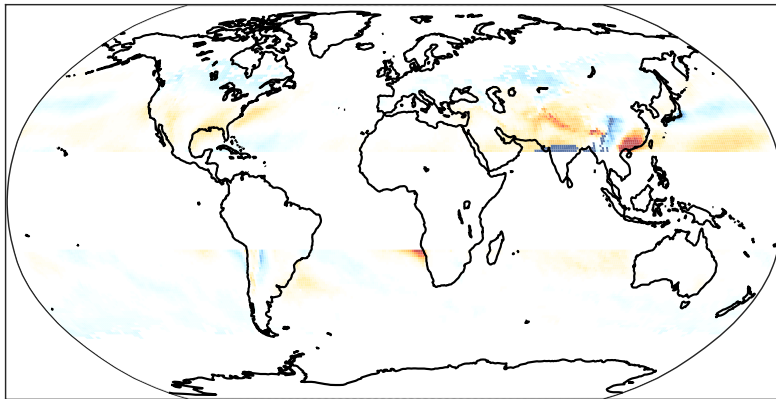


FIG. 5: (a) Seasonal time series of the downwelling surface solar radiation (black) measured at the University of Washington (UW ATG), Seattle and at (blue) the nearest gridpoint of the CERES data. Black dots show the individual daily mean values at UW ATG, the thin black line is the climatological mean for the calendar day and the thick black line is the spline fit. The shaded blue area is bounded by the maximum and minimum CERES values for the calendar day over the record (2000-2018), the thin blue line is the climatological mean for the calendar day and the thick blue line is the spline fit. The red line shows the (top of atmosphere downward) insolation from CERES. Vertical black and blue lines show the timing of the (spline fit) maximum and minimum surface solar radiation in the CERES and UW ATG data respectively and the vertical red lines show the summer and winter solstice. (b). Seasonal time series of the spline fit (black) UW ATG surface solar radiation and (green) T_{2m} at SEATAC. The inset shows the relationship between T_{2m} at SEATAC and (black) surface solar radiation at an optimal lead of 25 days and (red) top of atmosphere insolation at an optimal lead of 32 days.

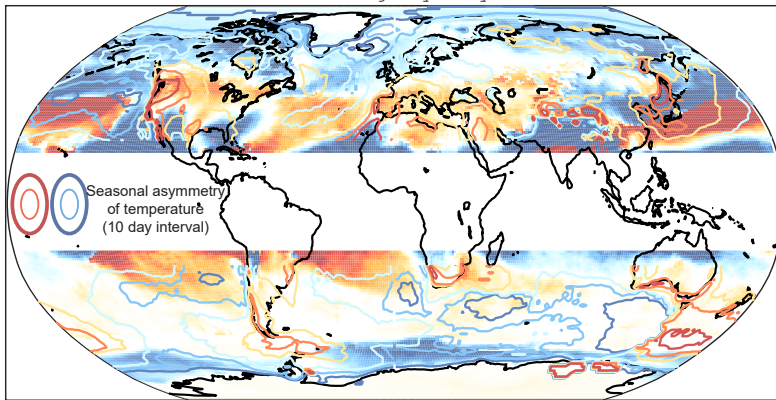
A Timing of maximum surface solar



B Timing of minimum surface solar



C Seasonal Asymmetry of Surface Solar



Timing relative to solstice (days)

Timing asymmetry (days)

FIG. 6: (a) Timing of maximum in surface solar radiation relative to the summer solstice from the CERES dataset. (b) Timing of seasonal minimum of surface solar radiation relative to the winter solstice. (c) Seasonal asymmetry of surface solar radiation defined as the difference between the top and middle panel. The contours show the seasonal asymmetry of surface temperature (ASYM) from the ERA surface data (repeated from Figure 3) with contour interval of 10 days using the same colorbar as the surface solar timing (zero contour is omitted). In panel (a), the inset shows the time series of downwelling surface solar radiation at two gridpoints straddling the strong north-south gradient in the North Pacific (marked by circles on the map) with timing of the maximum shown by the vertical lines.

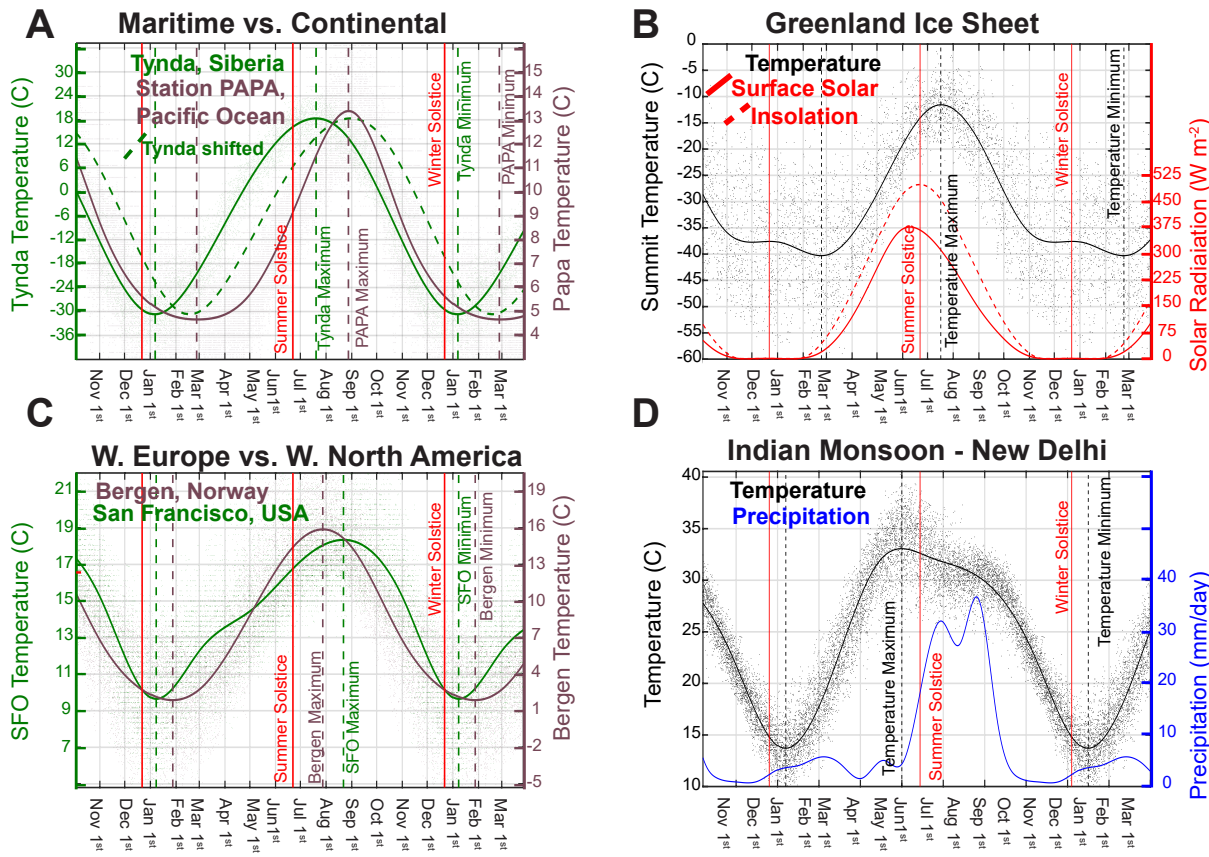


FIG. 7: (a) Comparison of the seasonal cycle of surface temperature at a typical continental location (Tynda, Siberia – green) and a maritime location (Weather Station Papa – purple). The maritime record has been rescaled by a factor of 6 (c.f. the left, green and right, purple y-axes) so that the seasonal cycles are visible on the same axis. Dots show the daily data and the lines show the spline fit to the data; vertical lines show the timing of the extrema. The dashed green line shows the continental record lagged by 42 days (such that the maximum are in phase) to highlight the different shapes of the seasonal cycle over land and ocean. (b) Seasonal times series of temperature (black) and solar radiation at the surface (dashed red) and insolation at TOA (solid red) at Greenland Summit Station. (c) As in panel B except a comparison on maritime climates in western North America (San Francisco airport, USA, green) and western Europe (Bergen, Norway, purple). (d) Seasonal time series of temperature (black) and precipitation (blue) at New Delhi, India.

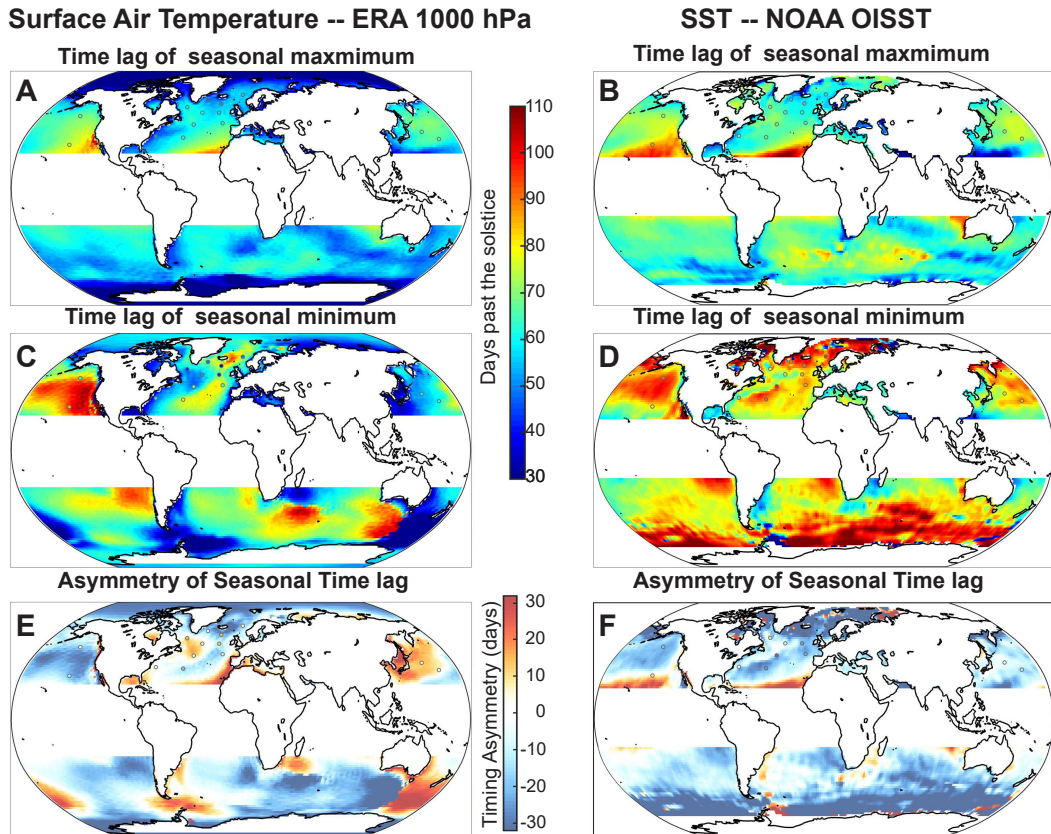


FIG. 8: Comparison of seasonal timing of T_{2m} and SST over the oceans. The left panels show τ_{MAX} , τ_{MIN} and ASYM defined from surface air temperature (from ERA 1000 hPa) and the right panels show the same quantities calculated from SST data (NOAA OISST). The dots show the ocean weather ship locations and are color coded by the timing of the station measured T_{2m} in the left panel and SST in the right panel.

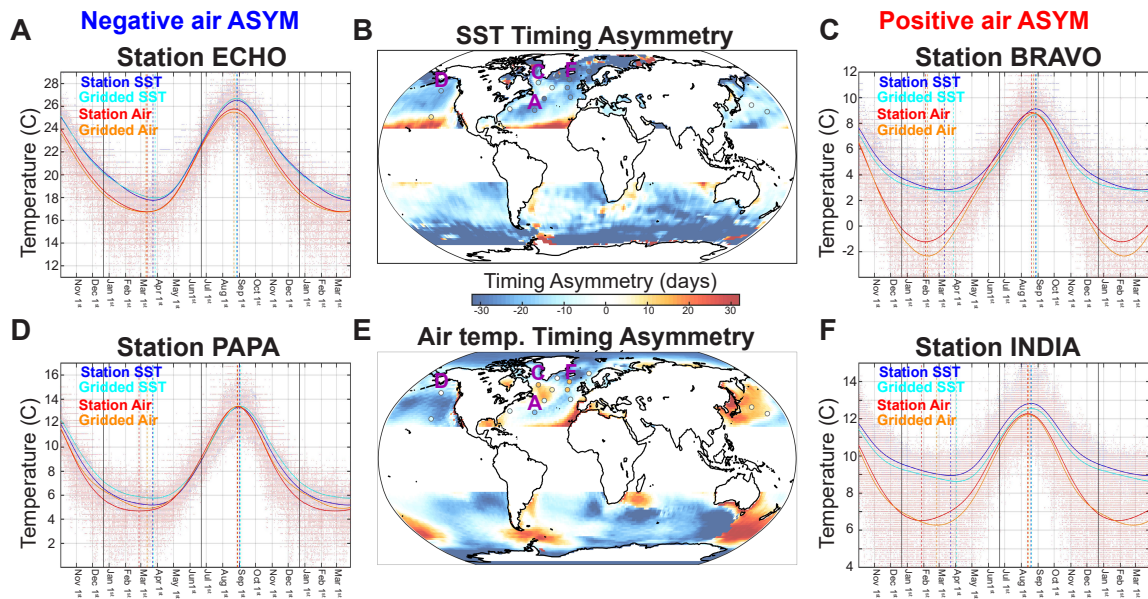


FIG. 9: (a,c,d,f) Time series of smoothed seasonal cycles of (blue) SST and (red) surface air temperature (T_{2m}) at selected OWS locations. The cyan line shows the NOAA OISST data and the nearest neighbor gridpoint. The orange line shows the ERA reanalysis T_{2m} data at the nearest neighbor gridpoint. The stations are organized by those with negative (positive) ASYM in T_{2m} on the left (right) and those where the timing is well (poorly) replicated in the gridded data on the top (bottom). The maps of ASYM defined from the SST data (NOAA OISST) and the ERA surface air temperature data respectively (previously shown in Fig. 8) are shown in panels b and e with the highlighted stations labeled by the letter of the panel they appear in (just above the station location) to orient the reader.

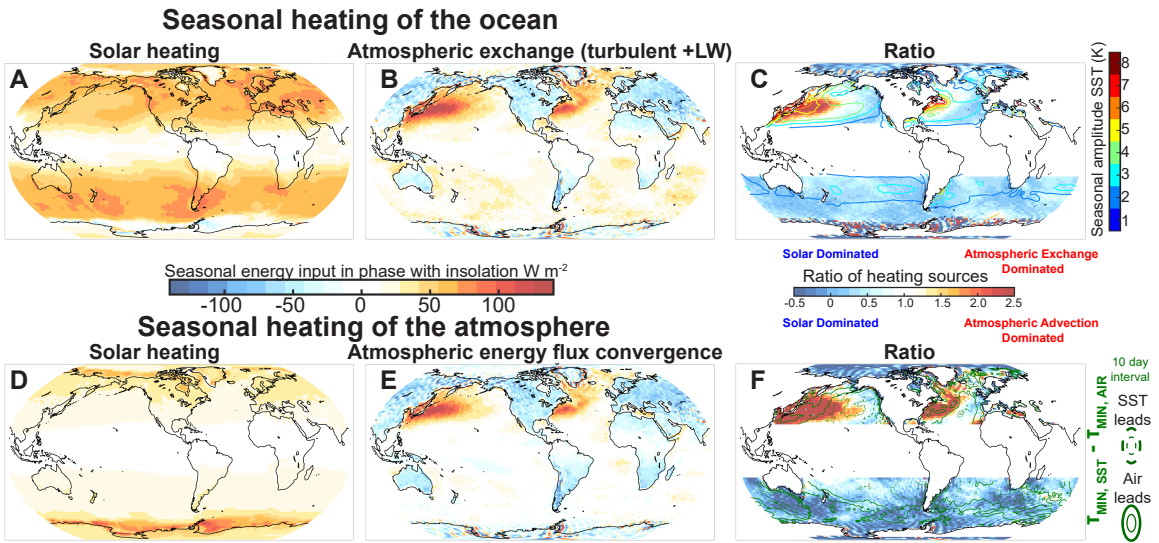


FIG. 10: The source of seasonal heating of the (top) ocean and (bottom) atmosphere defined as the seasonal amplitude of energy input phase with the insolation. The oceanic energy input is broken down into (a) surface solar radiation and (b) energy exchange with the atmosphere. Panel (c) shows the ration (atmospheric exchange divided by solar heating); the seasonal amplitude of SST is overlaid in contours. The atmospheric energy input is broken down into (d) solar radiation absorbed in the atmospheric column and (e) atmospheric energy flux convergence (advection). Panel (f) shows the ratio (advection to solar); the phase advance of the atmospheric minimum temperature relative to the SST minimum is shown in green contours.

Station ASYM compared to ERA ASYM

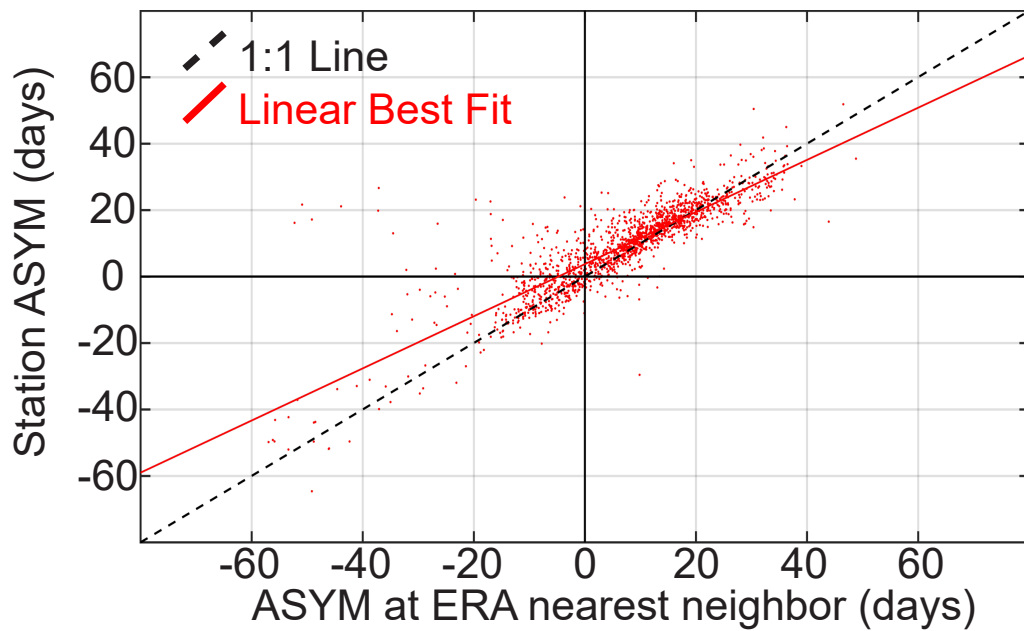
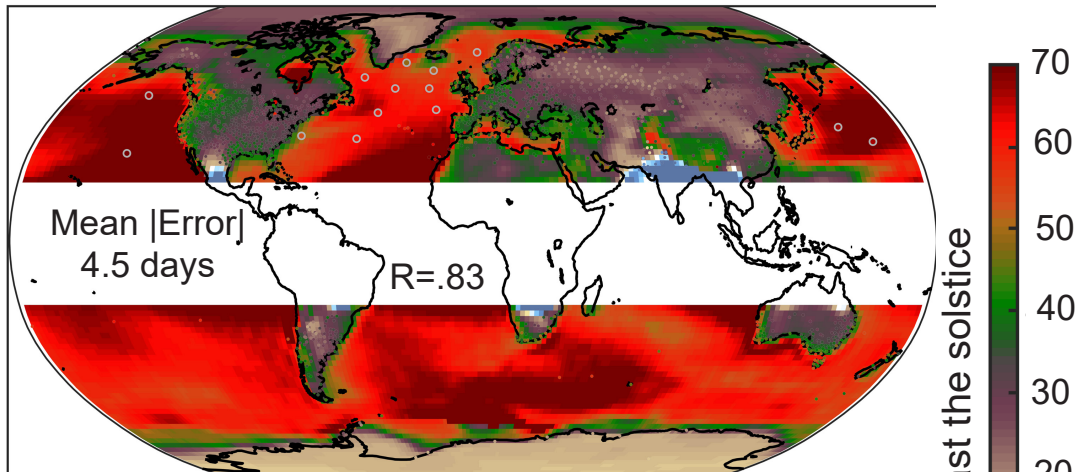
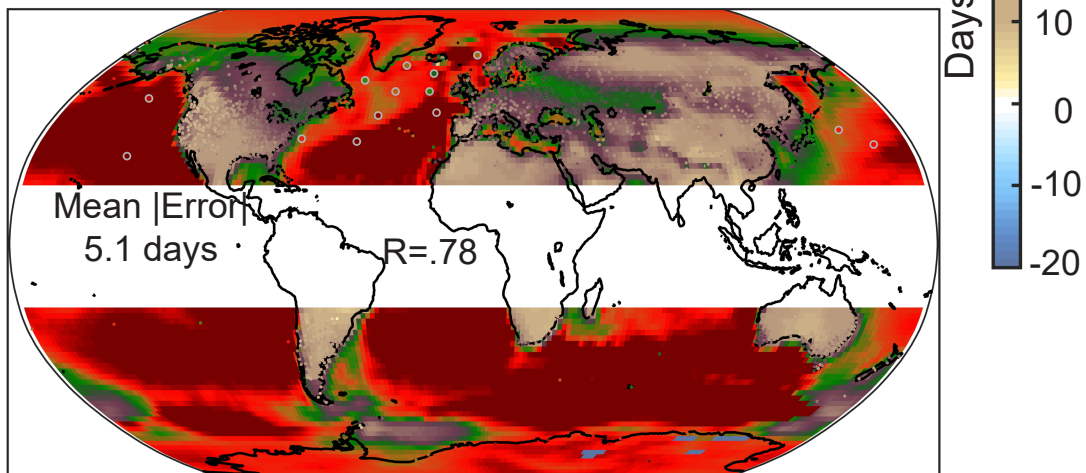


Fig. A1: Scatter plot of (ordinate) ASYM calculated from the station data versus (abscissa) the ASYM calculated from the ERA surface temperature at the nearest grid point. The dashed black line is the 1:1 line and the red line is the linear best fit.

A Time lag of seasonal maximum



B Time lag of seasonal minimum



C Asymmetry of Seasonal Time lag (A-B)

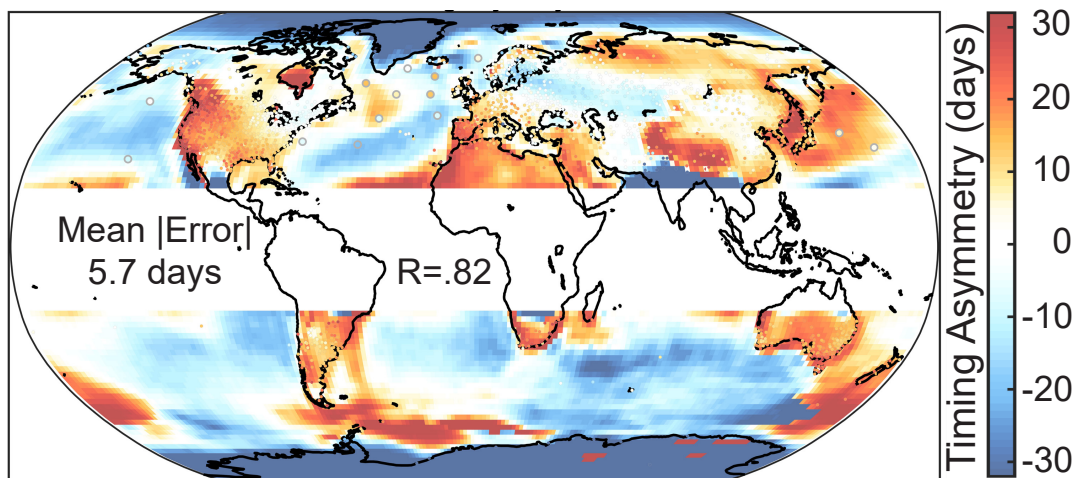


Fig. A2: As in Fig. 2 except for the NCEP reanalysis. (a) Time lag of seasonal maximum temperature relative to the summer solstice. Colors show results from the gridded 2 meter air temperature from the NCEP reanalysis and the individual dots show the location of the station data color coded by the time lag given by the common colorbar to the right. (b) As in (A) except for the time lag of the minimum temperature relative to the winter solstice. (c) The asymmetry in the timing of the seasons (ASYM), defined as (a) minus (b). This panel uses the colorbar on the lower right.

Seattle and Mt. Rainier Seasonal Cycle Temperature

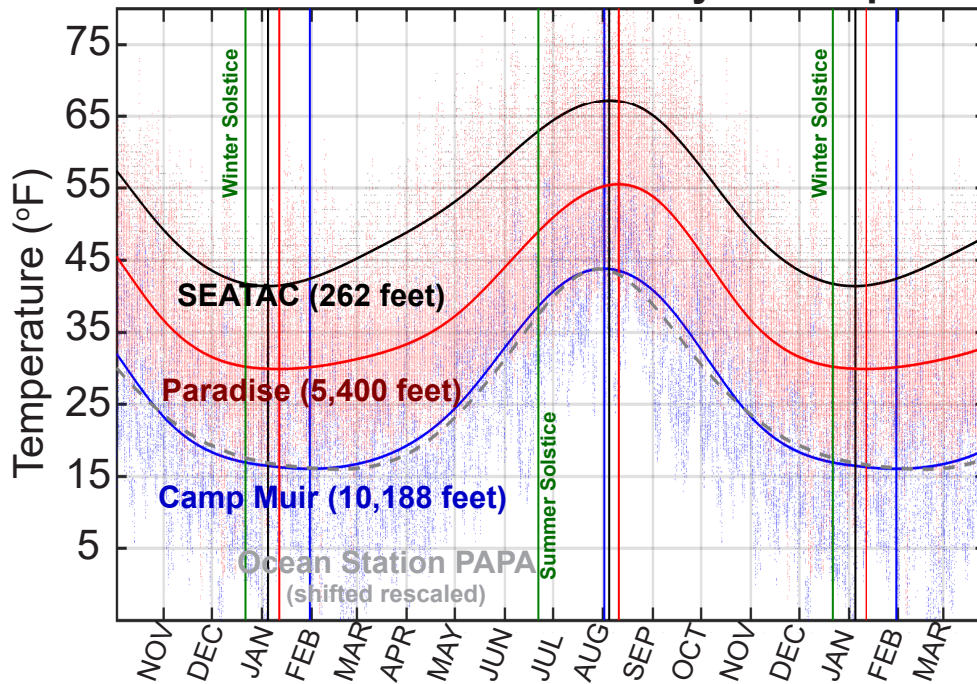


Fig. A3: Comparison of seasonal cycle of temperature on Mount Rainier at (red) Paradise (elevation 5,400 feet) and (blue) Camp Muir (elevation 10,188 feet) with that near sea level at (black) SEATAC. The gray dashed line is the seasonal cycle of SST at ocean station PAPA shifted and rescaled for visual comparison. The vertical lines indicate the timing of τ_{MAX} and τ_{MIN} in each time series given by the same color.

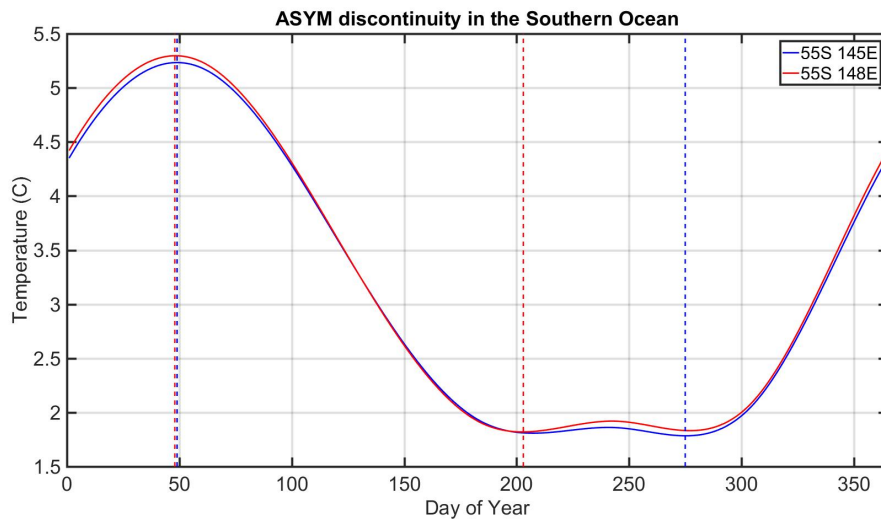


Fig. A4: Time series of ERA surface air temperature at gridpoints separated by 3° longitude spanning the discontinuity in ASYM south of Australia seen in Fig. 2c at 55°S . The blue time series is from 55°S , 145°E with $\text{ASYM} = -44$ days and the red time series is from 55°S , 148°E with $\text{ASYM} = +27$ days. The dashed vertical lines show the timing of τ_{MIN} and τ_{MAX} for the time series of the same color.

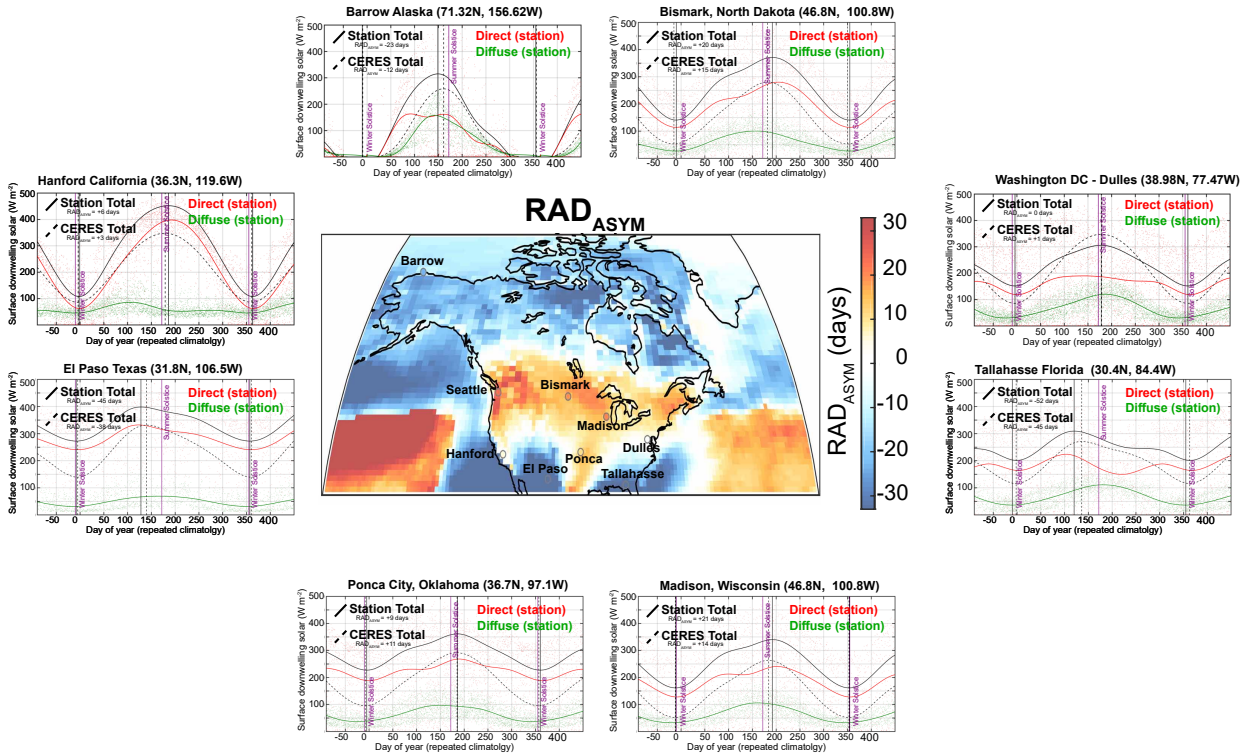


Fig. A5: Comparison of RAD_{MAX} , RAD_{MIN} and RAD_{ASYM} calculated in the gridded CERES data to that calculated using DSR measurements from the US (Sengupta et al. 2018). The dots show the observed daily mean DSR and the solid lines show the smoothed climatological seasonal cycle. The direct radiation is shown in red, the diffuse in green and the total observed DSR in black. The dashed black line shows the smoothed seasonal cycle of total DSR from CERES data at the nearest neighbor gridbox. Vertical lines show the time of RAD_{MAX} and RAD_{MIN} identified in the smoothed timeseries of the same linetype. The purple vertical lines show the winter and summer solstices. The inset map shows the RAD_{ASYM} values at each of the stations (colored dots circumscribed by gray) overlaid on (colors) RAD_{ASYM} calculated from the CERES DSR data.